**Title**

Self-extinguishing relay waves enable homeostatic control of human neutrophil swarming

**Permalink**

https://escholarship.org/uc/item/1nb516gt

**Author**

Strickland, Evelyn

**Publication Date**

2024

**Supplemental Material**

https://escholarship.org/uc/item/1nb516gt#supplemental

Peer reviewed|Thesis/dissertation

Self-extinguishing relay waves enable homeostatic control of human neutrophil swarming
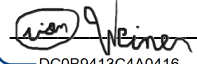
by
Evelyn Strickland

DISSERTATION
Submitted in partial satisfaction of the requirements for degree of
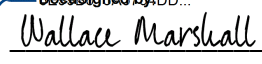DOCTOR OF PHILOSOPHY

in

Biophysics

in the

GRADUATE DIVISION
of the
UNIVERSITY OF CALIFORNIA, SAN FRANCISCO

Approved:

_____ Orion Weiner
                                          Chair

_____ Zev Gartner

_____ Wallace Marshall

_____

_____
                                          Committee Members

# Dedication

This work is dedicated to my Mom, Dad, Brother, and all my found family (particularly Brooke, Daniel, Julia, Lauren, Miranda, and Ryan) who helped me stick around long enough to see this through.

# Acknowledgements

I owe a huge debt to my PI, Orion Weiner, my lab, and all my friends who stuck with me through the chaos; I can't say enough really. I would also like to take the space to appreciate all the cats I fostered that kept me company when times were rough, even Oskar.

# Contributions

The work presented is the collective effort of a fantastic team of scientists. While the bulk of the conceptualization, experimentation, analysis, and writing was done by myself and Orion, the following people were also instrumental in the work presented here: Deng Pan, Ariel Amir, and Wencheng Ji for their work on the theoretical modeling and mathematics presented. Julia S. Kim for her experimental work that initially found the effect DPI has on swarming and calcium waves. Christian Godfrey, Alex Hopke, Michael Mansour, and Daniel Irimia for their work in helping develop and manufacture the swarming targets used. Christa S. Zerbe for her and her lab's help in collecting and shipping CGD patient samples.

# Epigraph

"The migrant has lost the nation state. The refugee has lost their house. The trans person loses their body. They all cross that border. The border is part of them and cuts through them. Usurps and overthrows them."

*- Can the Monster Speak?*

Paul B. Preciado

# Self-extinguishing relay waves enable homeostatic control of human neutrophil swarming

## Evelyn Strickland

## Abstract

Neutrophils collectively migrate to sites of injury and infection. How these swarms are coordinated to ensure the proper level of recruitment is unknown. Using an ex vivo model of infection, we show that human neutrophil swarming is organized by multiple pulsatile chemoattractant waves. These waves propagate through active relay in which stimulated neutrophils trigger their neighbors to release additional swarming cues. Unlike canonical active relays, we find these waves to be self-terminating, limiting the spatial range of cell recruitment. We identify an NADPH-oxidase-based negative feedback loop that is needed for this self-terminating behavior. We observe near-constant levels of neutrophil recruitment over a wide range of starting conditions, revealing surprising robustness in the swarming process. This homeostatic control is achieved by larger and more numerous swarming waves at lower cell densities. We link defective wave termination to a broken recruitment homeostat in the context of human chronic granulomatous disease.

# Table of Contents

# List of Figures

# List of Tables

# INTRODUCTION

During collective migration, individual organisms coordinate their movement to solve critical tasks. Birds flock, fish school, and insects swarm to escape predation, find food, and navigate complex environments efficiently.[1–3] These organismal collectives rely on individuals acting on local information such as external environmental cues, neighbor behaviors, or self-generated chemical cues to create complex emergent decisions. Collective migration is also organized at the cellular level, where groups of cells coordinate wound healing,[4,5] cancer metastasis,[6] multicellular morphogenesis,[7] and the transition from single-cell to multicellular existence.[8] While some examples of collective cell migration are well understood, such as *Dictyostelium* aggregation,[9–13] we lack a comparable understanding of the collective rules that organize the human immune response.

Neutrophils are first responders of the innate immune system that are recruited to sites of injury and infection to neutralize invading pathogens and aid in tissue repair.[14–16] Because the primary signals of injury/infection are relatively short-ranged, activated neutrophils release chemoattractants such as Leukotriene B4 ($LTB_4$) that act to augment the recruitment of additional neutrophils. This self-amplified 'swarming' process significantly enhances the speed and range of recruitment,[17–21] but this process must be tightly regulated to limit collateral damage.[17,22–24] While some brakes on swarming are known,[17,20,22] how neutrophils control the spatiotemporal dynamics of cell-cell communication to recruit the appropriate number of cells early in the swarming process is not well understood.

1

While many neutrophil swarming studies have been performed in living animals,[17,19,21,22,25–28] the *in vivo* context presents several challenges for mechanistic dissection of the swarming process. For example, multiple cell types modulate swarm initiation and propagation,[22] there are a multitude of diffusive signals following tissue damage,[21,22] and the *in vivo* migration environment is complex and difficult to image at high spatiotemporal resolution. These challenges make it difficult to mechanistically dissect the regulation of swarming. Furthermore, a focus on model organisms precludes the analysis of swarming for human neutrophils despite known differences in primary human neutrophil behaviors compared to model systems.[29,30] To address these limitations, we leverage an *ex vivo* assay to study human neutrophil swarming in response to controllable, reproducible, well-defined cues. This assay expands upon our previously-developed *ex vivo* swarming system[20,31] in which a defined grid of heat-killed *Candida albicans* "targets" are spotted on a thin slip of glass to act as an array of swarm initiation sites. Healthy human primary neutrophils isolated from whole blood are added to the assay, and swarming responses centered on the targets are observed with live cell microscopy.

# RESULTS

**Fast-moving multicellular Ca2+ waves define the zone of recruitment in human neutrophil swarming**

To monitor cell-cell communication in conjunction with more traditional swarming readouts like motility, we used a cytosolic calcium dye. Neutrophils increase cytosolic calcium following exposure to primary chemoattractants and swarming cues such as LTB$_4$,[32] and we envisioned that monitoring calcium influx would enable us to follow the propagation of swarming signals and correlate these to the regulation of directed cell movement (**Figure 1A**). Furthermore, calcium signals at the core of injury sites *in vivo* have been linked to key swarm signaling events,[19] and the simpler planar geometry along with the higher signal-to-noise imaging of our assay should enable a more sensitive detection of swarm signal propagation to neutrophils far from the heat-killed *Candida albicans* target. While calcium signaling has been studied during mice and zebrafish swarming,[19,27] it has not during human neutrophil swarming and a lack of quantitative tools for analyzing cell-cell communication has limited a deeper mechanistic dissection of the swarming process using this readout.

Following neutrophil introduction to the assay, we observe a calcium influx of the neutrophils that are in contact with the fungal target as well as multiple multicellular waves of calcium activity that radially propagate away from the target to surrounding neutrophils (**Video S1**). An example time course of these waves is shown in **Figure 1B** with the overlayed tracked boundary of the calcium wave. Wave tracks are calculated by fitting a circle to a cloud of cells that are determined to be active via calcium signal binning and grouped using the ARCOS algorithm[33] (**Figure S1A,B; Video S2**). Wave movement is

roughly isotropic, and the fitting of waves to a circle enables the tracking of wave propagation kinetics (**Figure S1C,D**). Immediately following the passage of a calcium wave, cells rapidly polarize and migrate radially towards the wave origin site. Cells within the wave perimeter move towards the fungal target, while cells outside the wave perimeter lack coordinated movement (**Figure 1C,D**). By analyzing cell responses across many targets and donors, we observe that most, if not all, movement occurs within the boundaries of tracked calcium waves, indicating that these wave fronts represent an effective boundary of the swarming guidance cue reception (**Figure 1E**). Though the propagating calcium waves delimit the zone of recruited neutrophils, they operate at very different timescales with respect to neutrophil movement. Calcium waves move an order of magnitude faster than the resulting neutrophil chemotaxis towards the wave origin (**Figure 1F**), and calcium waves propagate in an opposite direction to cell movement during swarming. The dramatically different timescales of calcium wave propagation and cell movement suggest that the movement of neutrophils does not play a significant role in the propagation of individual swarming waves.
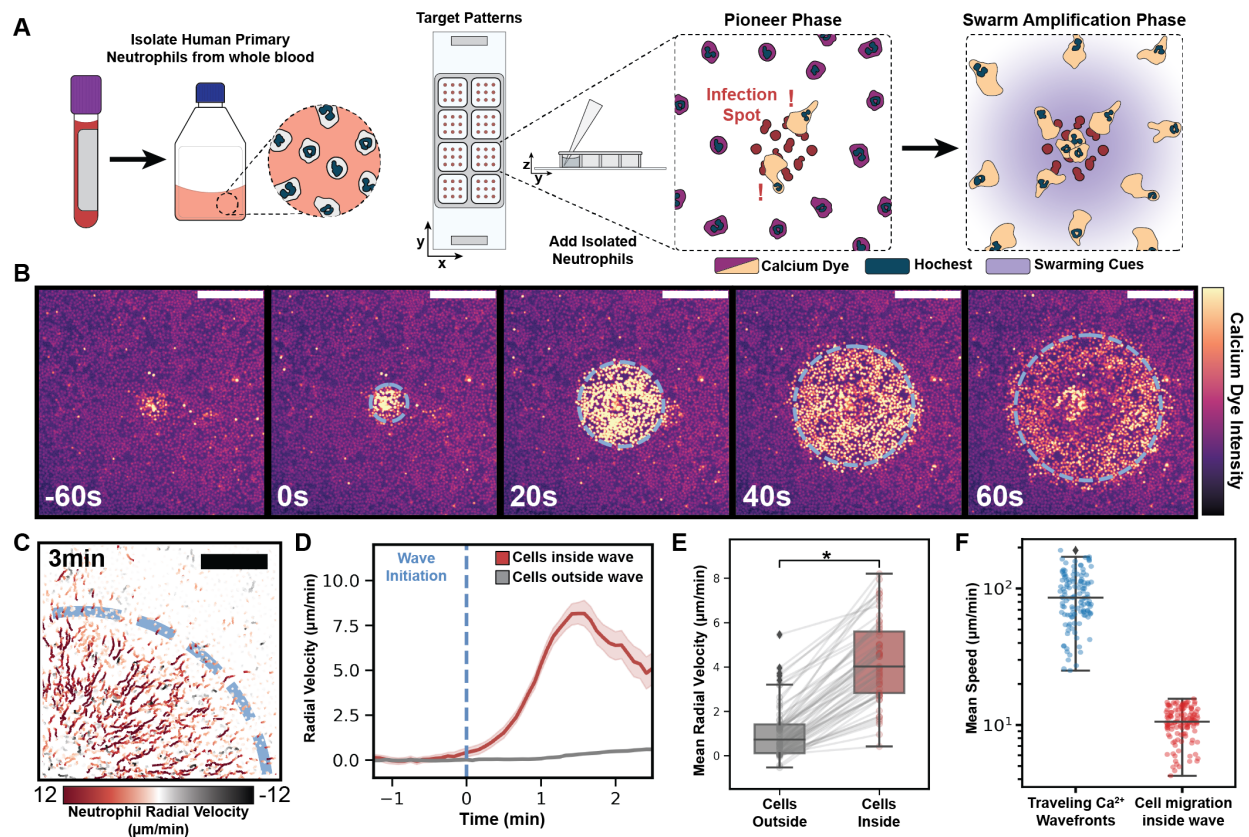
**Figure 1. Fast-moving multicellular Ca2+ waves define the zone of recruitment in human neutrophil swarming.** (**A**) *Ex vivo* assay for neutrophil swarming with self-amplified recruitment of cells in response to local site of heat-killed *Candida albicans*. Human neutrophils are isolated via immunomagnetic selection and dyed with CalBryte 520-AM (cytosolic $Ca^{2+}$ reporter, used to monitor neutrophil detection of pathogen and swarming cues) and Hoechst 3334 (nuclear marker, used to track cell movement). Cells are placed on printed targets of heat-killed *Candida albicans,* and neutrophil swarming responses are monitored via confocal microscopy. (**B**) Time-lapse sequence of a multicellular wave of neutrophil $Ca^{2+}$ activity following detection of the fungal target. The dotted line represents the wave boundary as tracked by our analysis software; Scale bar: 200 μm. (**C**) $Ca^{2+}$ wave defines the zone of neutrophil recruitment towards the fugal target. The final radius of $Ca^{2+}$ wave from cells in **B** is shown in blue. Cell tracks for 3 minutes following wave initiation are indicated with color corresponding to radial velocity towards the wave center; Scale bar : 100 μm. (**D**) Average radial velocity for cells inside versus outside the final wave boundary is plotted over 6 minutes for a population of cells during a single $Ca^{2+}$ wave (Cell tracks inside the wave n = 3720, outside wave tracks n = 9499). Wave boundary predicts zone of recruitment during swarming. (**E**) Comparison of mean radial velocity for cells inside versus outside the largest $Ca^{2+}$ wave boundary in each experiment. Tracks were averaged over the duration of the wave event, and lines connect mean radial velocities of outer versus inner (Figure caption continued on the next page.)

(Figure caption continued from the previous page.) cells for each experiment. Dependent paired t-test p-value = $5.8 \times 10^{-27}$; Target ROIs n = 56. (**F**) Average velocity of $Ca^{2+}$ waves propagated across the field of cells during swarming compared to the average cell velocity for the cells within these wave boundaries. Propagated $Ca^{2+}$ waves are approximately one order of magnitude faster than cell movement during swarming.

## Ca2+ waves are mediated by LTB4 and are consistent with active relay but not core production models

LTB$_4$, an inflammatory lipid of the leukotriene family, is thought to be one of the key secreted molecules that regulates neutrophil swarming.[20,21] Neutrophils release LTB$_4$ in response to various damage-associated pattern molecules and pathogen-associated pattern molecules,[20,34,35] including *Candida albicans*.[36] To test whether LTB$_4$ reception is required for the rapid long-range calcium waves in our *ex vivo* swarming assay, we blocked LTB$_4$ reception with the LTB$_4$ receptor antagonist BIIL315.[37] Blocking LTB$_4$ receptors inhibited the rapidly propagating long-range calcium waves that accompany swarming. In the absence of LTB$_4$ reception, a much smaller range, slow-moving Ca$^{2+}$ wave was observed (**Figure S2B,C; Video S3**). Quantitative analysis of wave propagation in both settings indicates that the rapid, long-range calcium waves that accompany swarming are dependent on LTB$_4$ reception (**Figure 2A**).

We next investigated how the LTB$_4$ ligands are propagated from the target site to the rest of the field. Two models have been proposed for the signal amplification observed during swarming. For the relay model of swarming, pioneer neutrophils at the site of infection secrete LTB$_4$, which activates surrounding neutrophils to synthesize and secrete additional LTB$_4$ and LTB$_4$ precursors, thereby continuing the relay.[21,34,35,38–43] This active relay mechanism could enable neutrophils to collectively signal across significant distances from the injury/infection site, analogous to cell-cell signal propagation in aggregating *Dictyostelium*.[44,45] In contrast, for the core production model of swarming, only neutrophils in direct contact with the site of injury/infection produce significant LTB$_4$, which then passively diffuses into the tissue to attract more neutrophils.[19] These two

swarming models give very different predictions for the dynamics of propagation of the LTB$_4$ wavefront as it moves away from the site of infection. The relay model predicts a wave that travels at a fixed velocity because of continuous signal re-amplification at the traveling front. This produces an activation zone whose area (wave fit circle radius squared -- R$^2$) scales quadratically in time. In contrast, since the core diffusion model predicts LTB$_4$ production restricted to a central source, this system is limited by diffusion, and therefore its activation area (R$^2$) scales linearly in time (**Figure 2B**).

Using this framework, we tracked the radius squared versus time for multiple waves across many healthy donors in control cells (**Figure 2C**) versus LTB$_4$-blockaded neutrophils (**Figure 2D**) and fit a power law to each individual wave trajectory. This analysis reveals that control cells exhibit an LTB$_4$ reception-dependent wave propagation with an alpha close to 2, consistent with the active relay model of swarming and inconsistent with the core production model of swarming (**Figure 2E**). Furthermore, upon fitting our observations to basic models of active relay and diffusion from a central source alone,[38] we find that the convex shape of the relay model best matches our early wave kinetics, further supporting relay as the mechanism of signal propagation (**Figure 2F**). In the absence of LTB$_4$ signal reception, cells exhibit a slower, shorter-range pattern of signal propagation with an alpha close to 1 (**Figure 2E**), consistent with core diffusion alone. These data suggest that the residual release of non-LTB$_4$ swarming ligands, such as IL-8,[20] from cells on the target create a shallow, diffusive gradient with limited chemoattraction (**Figure S2C**). These residual waves are best fit with a central diffusive model, and have a radius squared relation to time that appears linear (**Figure 2G**). These two examples establish that we can distinguish between diffusive waves and relay-

mediated ones, and that LTB4 receptor-mediated waves exhibit relay-like, ballistic spreading in the early phase of wave propagation.
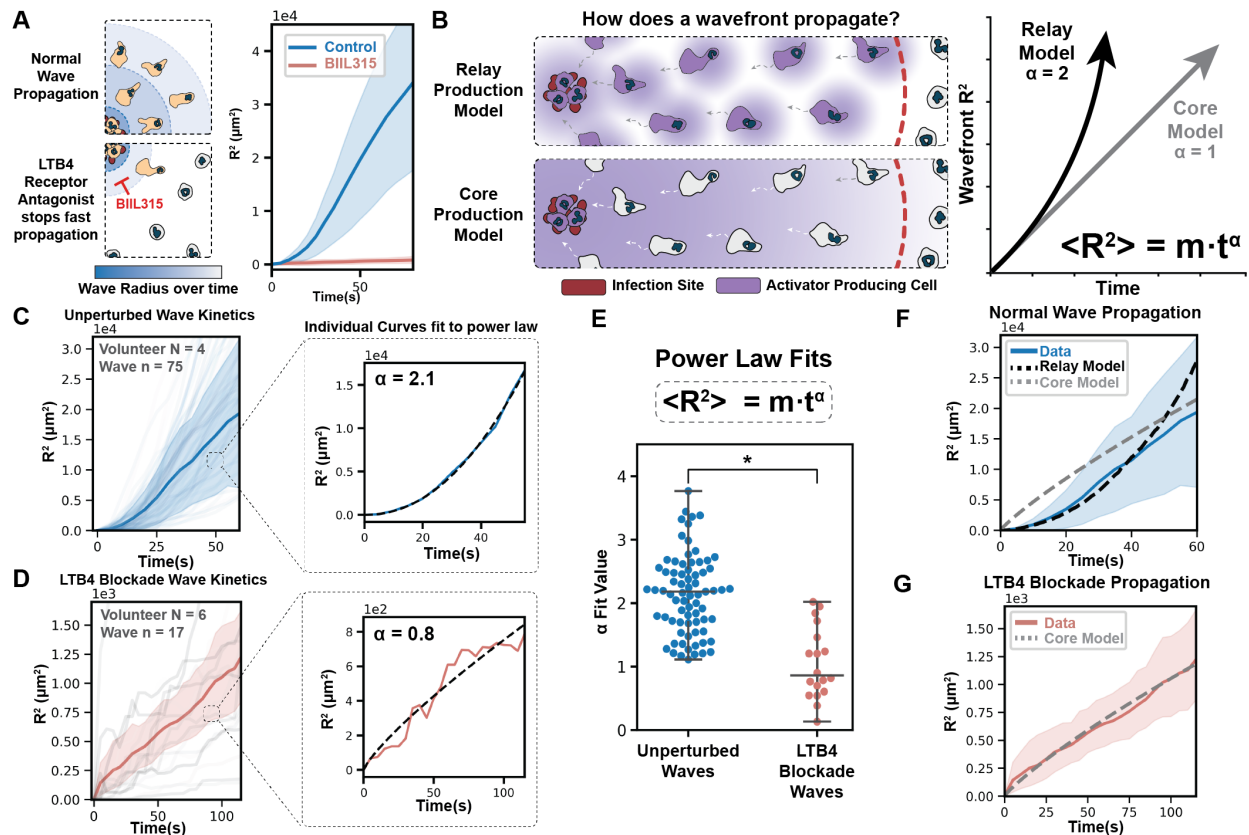
**Figure 2. Ca²⁺ waves are mediated by LTB₄ and are consistent with active relay but not core production models.** (**A**) Ca²⁺ wave propagation across a field of neutrophils during swarming for cells in the absence (50 waves) or presence (17 waves) of an LTB₄ receptor inhibitor (1 μM BIIL315); averages shown with 95% confidence interval shaded. LTB₄ reception is required for rapid, long-range Ca²⁺ wave propagation. (**B**) Two proposed models of LTB₄ propagation from a site of infection to the rest of the field with the predicted kinetics of signal propagation shown for each. In a relay model of swarming,[21,34,38] each activated neutrophil releases LTB₄, which stimulates the adjacent cell to release LTB₄; this wave should spread with a constant velocity over time, giving an alpha of 2. For a core production model of swarming,[19] only neutrophils at the center of a swarm produce LTB₄, which moves across the field through passive diffusion; this wave should spread with an alpha of 1 (linear on R² plot). (**C**) Average early wave kinetics for control cells with mean and 95% confidence interval. Individual tracks are fit to a power law equation to determine the alpha of wave propagation for each experiment. (**D**) Wave propagation for LTB4R-inhibited cells averaged with 95% confidence interval are individually fit to a power law equation for the first two minutes following swarm initiation. (**E**) Resulting curve fit alpha parameters for both unperturbed and LTB4R blockade conditions are plotted, with control cells showing wave propagation consistent with active relay. LTB₄ reception-inhibited cells showed residual wave propagation consistent with core diffusion. Welch's t-test P-value = (Figure caption continued on the next page.)

**10**

(Figure caption continued from the previous page.) $4.0 \times 10^{-8}$. (**F**) Same data as **C** replotted and fit to a simple relay model.[38] For the core diffusion model to match the final radius mean at 60 seconds, its early kinetics must outpace the experimental data, allowing us to exclude core production as the dominant mechanism of wave propagation. In contrast, our experimental data is consistent with active relay. (**G**) Same data as **D** replotted and fit to the core model. The shape of the model curve gives a good agreement with our data in this case, indicating that following $LTB_4$ receptor blockade, residual swarm cues diffuse away from a central source by passive diffusion and not active relay.

**Swarming relay waves self-extinguish through an NADPH Oxidase based negative feedback mechanism**

Our observation that neutrophil swarming cues radiate from heat killed yeast targets via active relay might be expected to produce waves that continue to propagate as long as there are nearby receptive cells to continue the wave. This is the behavior of actively relayed systems including action potentials, mitotic waves, and *Dictyostelium* aggregation.[46] We previously proposed an active relay model for swarming in which cells that pass a threshold amount of $LTB_4$ themselves create more $LTB_4$, as shown in **Figure 3A**.[38] Once initiated, these waves continue to propagate indefinitely given a field of responsive cells. In contrast with the predictions of a simple relay model, our experimentally-observed waves propagate and then abruptly stop (**Figure 3B,C**), indicating a more complex mode of regulation than positive feedback alone.

Since there are multiple circuits that negatively regulate the production of $LTB_4$,[47–50] we envisioned one of these negative feedback circuits could collaborate with $LTB_4$ positive feedback to enable self-termination of neutrophil swarming waves. What might serve as the activation-dependent inhibitor in this self-extinguishing relay mechanism? The inhibitor should be activated downstream of $LTB_4$ reception, and the effect of this inhibitor should attenuate $LTB_4$ production. NADPH oxidase activation satisfies both conditions. NADPH oxidase is used in ROS-dependent pathogen killing downstream of $LTB_4$,[31,48,51] and the inhibition of NADPH oxidase activation potentiates LTB4 production and neutrophil accumulation during swarming.[31,48,52–54] If NADPH oxidase activity is a critical component in self-extinguishing relay, we would expect NADPH oxidase inhibition

to prevent swarming wave termination, thereby enabling the circuit to appear more like a simple relay system (as in **Figure 3A**).

Indeed when compared to unperturbed waves, cells treated with the NADPH oxidase inhibitor DPI produce a single swarming wave that does not self-extinguish and instead continues to propagate from the target out of the ROI (or until colliding with another propagating wave) (**Figure 3E,F, S3E; Video S4**). Because DPI affects cell-autonomous roles of NADPH oxidase activity (like membrane depolarization)[55–57] as well as the potential paracrine roles of released ROS,[58,59] we next investigated the role of extracellular ROS through the use of ROS scavengers catalase and superoxide dismutase. This extracellular ROS inhibition did not elicit a significant change in wave stopping behaviors nor maximum wave size (**Figure 3G**). In contrast, DPI drugged cells produce convex wave kinetics that are consistent with a simple relay model within the entire boundary of the largest ROI possible for both targets spaced 1mm and 1.5mm apart (**Figure 3H; S3D,E,F,G**). These results suggest a cell-autonomous role of NADPH oxidase activation in LTB4 production, consistent with previous reports.[48] To ensure that this effect on wave dynamics is not an off-target of DPI, we analyzed neutrophils from Chronic Granulomatosis Disease (CGD) patients who have a genetic defect in neutrophil NADPH oxidase machinery.[53] Similar to DPI-treated healthy donor cells, CGD neutrophils also exhibit non-extinguishing wave dynamics within our largest possible ROI (**Figure S3B**). While both DPI-inhibited cells and CGD cells elicited strong recruitment within a calcium event, they only generate a single large wave compared to the multiple waves observed in unperturbed, healthy cells (**Figure S3C; Video S4**).
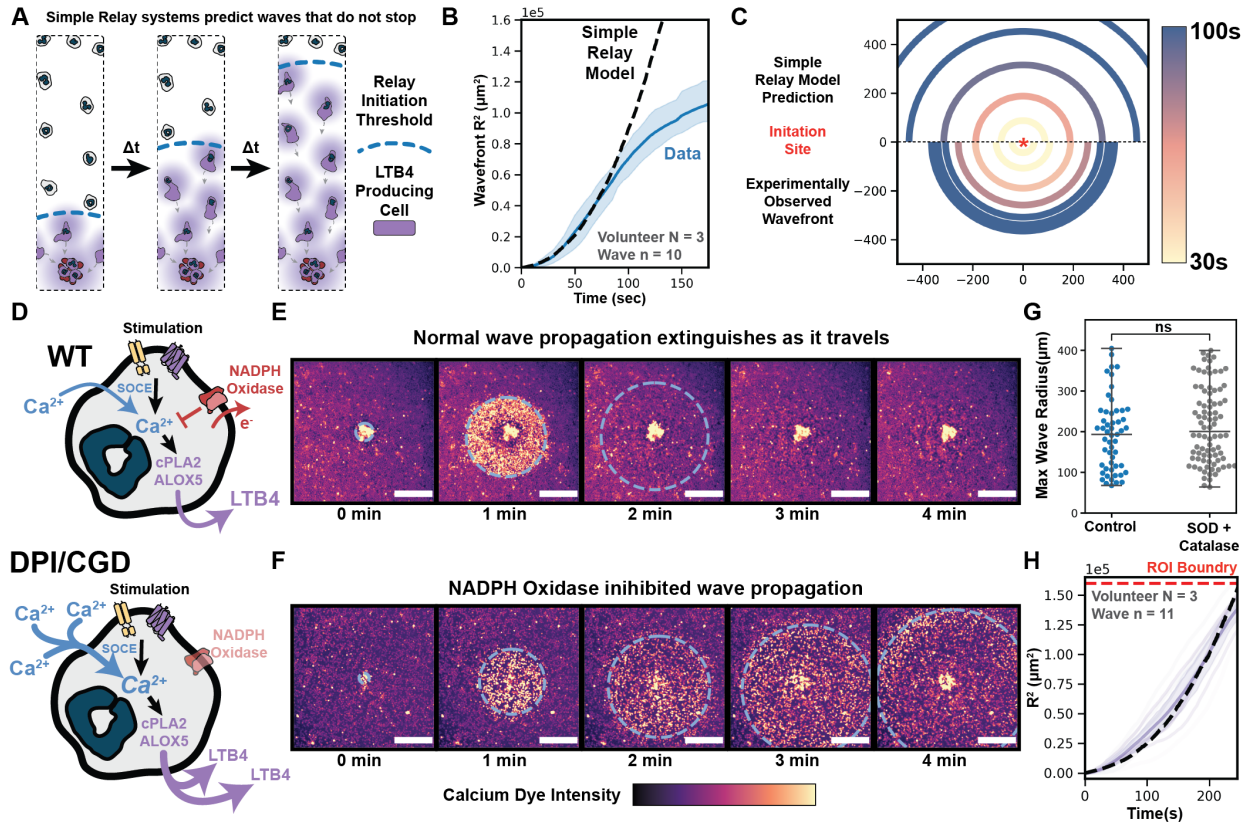
**Figure 3. Swarming relay waves self-extinguish through an NADPH Oxidase based negative feedback mechanism.** (**A**) Our previously-proposed simple diffusive relay model of swarming.[38] As cells exceed a threshold amount of extracellular LTB4, they begin to release more LTB4 to their surroundings, thereby activating adjacent cells to continue the relay. This wave propagates indefinitely once initiated in a homogenous field of cells. (**B**) While experimental waves initially propagate with a relay-like $R^2$ relation, in the latter phase the waves decelerate then stop. (**C**) Comparing the simple diffusive relay prediction with an average of experimentally observed swarming wavefronts shows how wave behavior diverges from experiment. Experimental relay waves come to a stop (bottom), whereas simple relay propagates indefinitely (top); Axes in μm; Wave n = 5. Volunteer N = 2. (**D**) NADPH Oxidase activation normally limits calcium influx which in turn reduces LTB4 production.[48] Inhibition of NADPH Oxidase activation removes this brake on calcium influx and LTB4 production. (**E**) Time lapse sequence of a representative $Ca^{2+}$ wave for unperturbed neutrophils. Dotted line represents tracked wave boundary. Boundary line is removed when the wave terminates and dissipates; Scale bar: 200 μm. (**F**) Time lapse sequence of a representative $Ca^{2+}$ wave for cells treated with NADPH oxidase inhibitor (50 μM of DPI for 15 minutes) before seeding in assay. Dotted line represents tracked wave boundary that, unlike control cells, continues to propagate beyond the field of view (~400 μm from target); Scale bar: 200 μm. (**G**) Sequestration of extracellular ROS through (Figure caption continued on the next page.)

(Figure caption continued from the previous page.) addition of human SOD (200U/mL) and human Catalase (>200U/mL) to the swarming assay does not appreciably change wave termination behaviors. In conjunction with the DPI experiments, our work supports the role of cell-intrinsic activation of NADPH oxidase for wave termination. Wave n = 137, Volunteer N = 3. Welch's t-test P-value = 0.16, ns. (**H**) Inhibition of NADPH oxidase activity via the NADPH oxidase inhibitor DPI (50 µM) produces swarming waves that no longer stop in the observable microscopic field and mimic simple relay dynamics throughout their propagation (Volunteer N = 3, Wave n = 11).

**A new class of models for self-extinguishing relay based on a positive feedback active relay coupled with an activation-dependent non-diffusible inhibitor**

We next sought to mathematically model potential circuit architectures that could account for the observed self-extinguishing neutrophil swarming waves. The first architecture we explored involved a *diffusive co-permissive cue* released at the core. This model was quickly discarded due to its dependence on a biologically implausible diffusion coefficient and its inability to explain the lack of wave termination following NADPH oxidase inhibition (See **Supplementary Modeling Text, Figure S4H,I,J**).

Turning our attention to potential inhibitory circuits that could underly a self-extinguishing relay, we found one prior example of a self-extinguishing relay model attempting to explain the spatial regulation of blood clotting. In this work, a 1D model of two separately-relayed, *diffusive activator and diffusive inhibitor* cues generated a fixed radius of relayed activation in a cell-free system.[60] We explored whether this model could create wave stopping solutions in 2D and 3D diffusive environments and were unable to find stable solutions for the diffusive conditions in our assay (**Supplemental Modeling Text**). Furthermore, this class of models requires a diffusible inhibitor and is therefore incompatible with the cell autonomous role NADPH oxidase activation plays in LTB$_4$ production (**Figure 3G**).[48]

To address these deficiencies in both model classes explored, we constructed a new mathematical model based on a *diffusive activator cue and a non-diffusive local inhibitor* that is consistent with our understanding of neutrophil self-extinguishing relay waves. Our model relies on a single diffusive ligand that triggers different cellular responses at two different threshold concentrations of the ligand (**Figure 4A**). This idea

is inspired by previous work showing that $LTB_4$ can evoke different cellular responses at different ligand thresholds.[61–65] In particular, BLT1 has been shown to exhibit a 'stepwise' phosphorylation pattern that allows the receptor to selectively trigger different arms of the GPCR signaling cascade at low (10nM) and high (100nM) amounts of LTB4.[64,65] In our self-extinguishing relay model, cells exposed to a low threshold of activating ligand ($L_1$) initiate a non-diffusive, local inhibition circuit that starts to limit the potential of that cell to create more activating ligand. This low threshold for negative feedback is consistent with previous reports of sub-nanomolar amounts of $LTB_4$ inhibiting further $LTB_4$ production in human neutrophils.[49] When the cell is exposed to a higher threshold of activating ligand ($L_0$), it begins to create more activating ligand locally if the local inhibition has not yet exceeded some amount (I). This local creation of ligand serves to help trigger neighboring cells to further relay the activating cue and is the basis for positive feedback in the system. This higher threshold for positive feedback is consistent with higher doses of $LTB_4$ shown to activate and augment key steps in $LTB_4$ synthesis/release.[35,39] Our current model is likely an oversimplification of the true positive feedback present, which likely involves a feedforward cascade in which $LTB_4$ generates and mobilizes arachidonic acid, which then acts in conjunction with $LTB_4$ to further $LTB_4$ synthesis.[40,42,43]

For our self-extinguishing relay model, we can expand on the analysis for traveling wave solutions first explored in previous work[38] to find four distinct phases for waves that have self-extinguishing relay behaviors. In **Figure 4B**, the initiation of a wave event begins with the low threshold for inhibitor circuit initiation (spatially drawn as $r_1$) spaced closely to the higher threshold for activator production (spatially drawn as $r_0$). As a result, for cells close to the target, only a small amount of inhibition is generated before cells

**17**

cross the threshold for activator production and effective activator cue relay occurs. For each relaying cell that has crossed both the $r_1$ and $r_0$ threshold of activator, the intracellular inhibition continues until an inhibitory max threshold value (I) is reached, stopping the production of further activating cue. This shutoff effect creates a time-delayed zone of cells that are no longer able to relay (spatially drawn as $r_2$). Because the inhibition circuit limits relay behind the propagation front, cells participating in the relay do so in a pulsatile manner. At increasing distances away from the target, the relay threshold is passed closer in time to the cellular shutoff event, limiting the window for activator production until the effective 'pulse duration' falls below a critical value; thereby terminating active relay at the wavefront (**Figure S4B**).

Consistent with our experimental observations, both continuous and discrete agent-based models generate fields of diffusive activating cue that propagate via a relay that has self-terminating properties (**Figure 4C, S4F, Video S7**). Our model also shows a good agreement with experimentally observed relay propagation kinetics, stopping behavior, and final max radius values (**Figure 4D**). By turning off inhibition in our model, we can recover simple relay propagation solutions like those observed in DPI treated cells and CGD patient cells (**Figure S4G, Video S7**). In our formal analytical treatment of the continuous model, we identify key mathematical conditions that are necessary to generate self-extinguishing solutions and demonstrate the stability of the modeling parameters (**Supplemental Modeling Text; Figure S4C,D,E**).
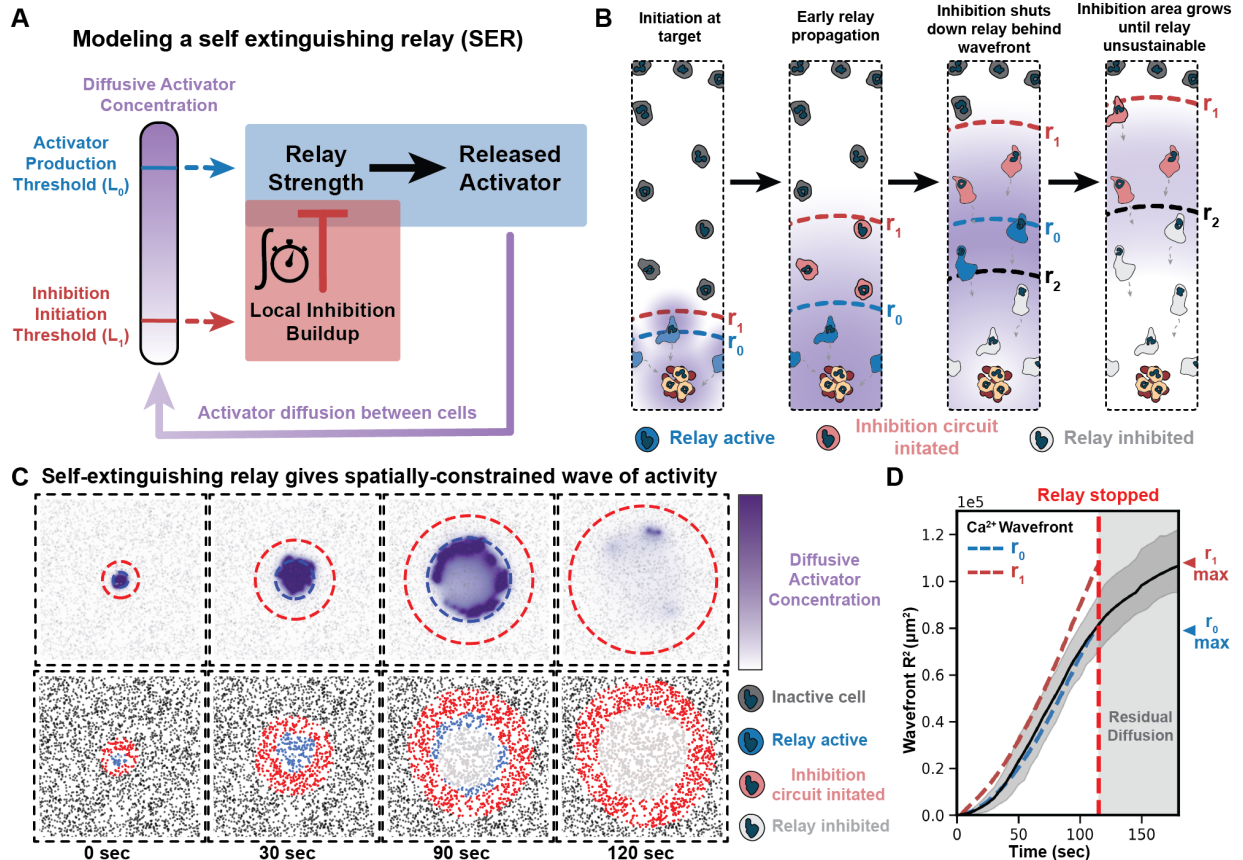
**Figure 4. A new class of models for self-extinguishing relay based on a positive feedback active relay coupled with an activation-dependent non-diffusible inhibitor.** (**A**) In this model, a single diffusive ligand propagates through a field of cells. At a low threshold of this extracellular ligand, cells initiate a non-diffusive local inhibition circuit that limits the relay potential of a given cell; once this inhibition accumulates to a critical level, cells lose their ability to participate in relay. At a higher threshold of the extracellular ligand, cells begin to emit more of the activating ligand unless the inhibition has accumulated to a sufficient level to block this process. (**B**) Based on the dynamics of ligand (purple) diffusion, the wavefront corresponding to the low inhibitory threshold ($r_1$, dotted red line) moves more rapidly than the wavefront corresponding to the high activating threshold ($r_0$, dotted blue line). Because of the difference in propagation speeds between the two thresholds, cells further from the target have longer periods of inhibition buildup (red cells) before initiating positive feedback (blue cells), dampening the relay strength as it moves away from an initiation site until the relay eventually terminates. As the inhibitory circuit reaches a shutoff threshold value (*I*), a zone of deactivated cells (indicated by $r_2$, light grey cells) grows behind the wavefront, ultimately overtaking and destabilizing further wave propagation. Non-activated cells are in dark grey. (**C**) Discrete simulations of this model yield a wave of propagating extracellular ligand that moves by active relay close to the initiation site before attenuating and eventually terminating. Diffusive activator gradient (purple) plotted (Figure caption continued on the next page.)

(Figure caption continued from the previous page.) with $r_0$ (blue) and $r_1$ (red) overlayed (top panels). Cell state plotted for same simulation as top panels to demonstrate how activated cells evolve from relaying to shutting off and terminating further relay propagation (bottom panels). (**D**) Because our cellular readout is calcium and not receptor activation, we predict that a calcium pulse occurs between the low ($L_1$) and high ($L_0$) thresholds of our model. Our model generates simulations that match both early wave relay kinetics and predict the final wave radius as being within the $r_1$ lower threshold boundary after relay shutoff and residual diffusion dominates late wave propagation. Experimental data taken from a subset of similarly-sized waves with similar propagation kinetics averaged over time with 95% confidence. Wave n = 5. Volunteer N = 2.

**Neutrophils tune the size and number of swarming waves in response to differences in initial cell density**

To investigate the physiological significance of multiple self-extinguishing waves, we next sought to probe the relation between wave size/number and the resulting cell movement and recruitment towards a target. We hypothesized that these wave parameters may be actively adjusted to enable robust homeostatic control of neutrophil recruitment across a wide range of initial conditions. First, we analyzed cell movement following a single well-separated wave event. Single-cell tracks were aligned based on the time at which they entered the wave to determine the average radial migration velocity profile (**Figure 5A; Unaligned track averages: Figure S5A**). Upon entering a wave, neutrophils execute a discrete 'run' of movement towards the wave center and then revert to random, slower movement, similar to the responses of *Dictyostelium* to waves of cAMP during aggregation.[11,66] Such a 'step' of movement inwards is consistent with the expected behavior from our self-extinguishing model where the chemotactic gradient decays behind the wavefront as the relay becomes dominated by the local inhibitory mechanism. These data indicate that a single wave event does not recruit all cells to the center in one burst. To expand our analysis to multiple waves, we integrated the radial movement of all cells within a wave event around a single target (**Figure 5B; S5B**). Each wave elicited the recruitment of a group of neutrophils toward a given target, with larger wave events more potently recruiting cells compared to smaller wave events (**Video S5**). When analyzed across many experiments and donors, the total integrated wave area correlated strongly with the Integrated Radial Movement of the cells within wave events (**Figure 5C**).

To investigate how swarming responses depend on starting conditions, we next varied the initial cell seeding density in our assay. At lower cell densities, there is an increase in the integrated calcium signaling area across all waves emanating from a single target (**Figure 5D**). As seeding density increases, neutrophils attenuate swarming responses by limiting both the size and number of waves emitted from a given target (**Figure 5E,F; Video S6**).
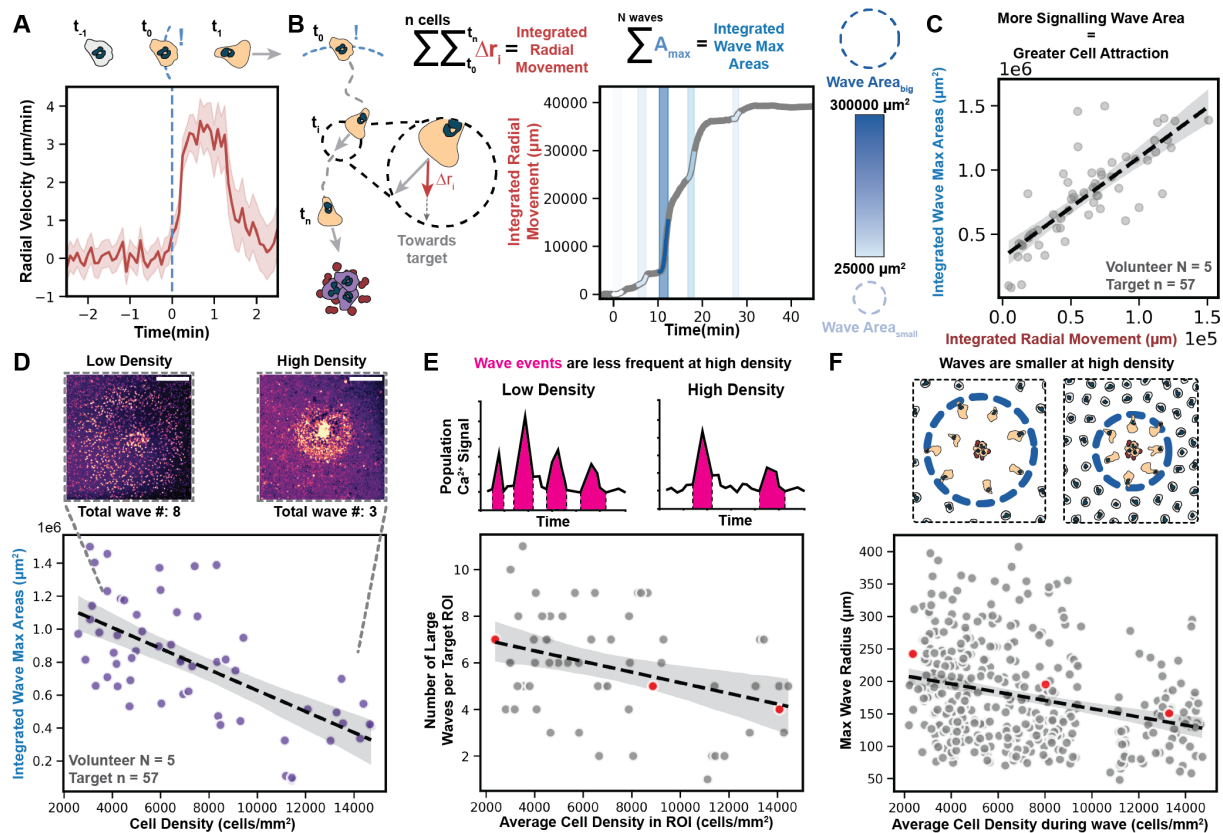
**Figure 5. Neutrophils tune the size and number of swarming waves in response to differences in initial cell density.** (**A**) Averaged radial velocities of neutrophil movement towards a target following time of exposure to swarming $Ca^{2+}$ wave with 95% confidence interval plotted for 1758 cell tracks. A single wave produces a transient bolus of neutrophil recruitment. (**B**) All cellular tracks inside a wave are integrated for their radial movement (Cell track n = 5813); multiple $Ca^{2+}$ wave events for the same target are plotted as shaded areas colored by maximum final area for an example ROI. Each wave induces a bolus of neutrophil movement towards the target, with larger waves inducing larger neutrophil responses. (**C**) Integrated radial movement of all cell tracks and integrated wave max area measurements calculated across 57 target ROIs demonstrate the strong positive correlation between $Ca^{2+}$ wave signaling area and movement towards a target. Linear fit slope: 7.8 μm +/- 0.8, 95% confidence interval. A control where all cell tracks are considered is in **Figure S5C**. (**D**) Relation of seeding density to cell accumulation at target. Integrated wave max area measurements taken for each target ROI over 45min. Linear fit slope: $-6.3 \times 10^4$ μm$^2$ per 1000 cells/mm$^2$ +/- $1 \times 10^4$, 95% confidence interval. Lower cell densities elicit larger and more numerous swarming waves; representative panel insets scale bar: 200 μm. (**E**) The number of waves emanating from a given target are inversely correlated with the seeding density of cells surrounding the target. Linear fit slope: -0.2 waves per 1000 cells/mm$^2$ +/- 0.07, 95% confidence interval. Red dots refer to representative $Ca^{2+}$ traces in **Figure S5D**. (**F**(Figure caption continued on the next page.)

23

(Figure caption continued from the previous page.)) The maximum radius of waves emanating from a given target are also inversely correlated with the seeding density of cells surrounding a target. Linear fit slope: -6.4 mm per 1000 cells/mm$^2$ +/- 1.0, 95% confidence. Red dots refer to representative Ca$^{2+}$ waves in **Figure S5E**.

**Healthy neutrophils exhibit robust homeostatic recruitment that is broken in CGD patient neutrophils**

We next investigated whether the tuning of wave size and number enables consistent levels of neutrophil accumulation across a range of initial cell densities. For this purpose, we assayed the kinetics of neutrophil accumulation and swarming wave responses for a range of starting cell densities (**Figure 6A**). At low seeding densities, we observed multiple large waves underlying swarming and accumulation of cells at the target. At higher seeding density, we observed similar accumulation at the target, but this is achieved by fewer and smaller waves (**Figure 6B**). This near-constant recruitment over a range of starting densities suggests homeostasis in the swarming response. To extend this observation, we quantified neutrophil recruitment to similarly sized sites of heat-killed *Candida albicans* over a six-fold range of seeding densities after 60 min (**Figure S6B**). Across this range of starting conditions, there was a near constant accumulation of neutrophils at the target, with targets at the lowest densities attracting approximately 85% of the cells attracted at the highest cell densities (compared to six-fold differences that would be expected for a non-homeostatic proportional system) (**Figure 6C,D; Figure S6C**). Because CGD patient neutrophils are defective in the negative feedback circuit that is needed to constrain wave size, we predicted that these cells should exhibit a defective homeostat and therefore recruit cells more proportional to their starting density; this is indeed the case (**Figure 6E,F; S6D, E**).
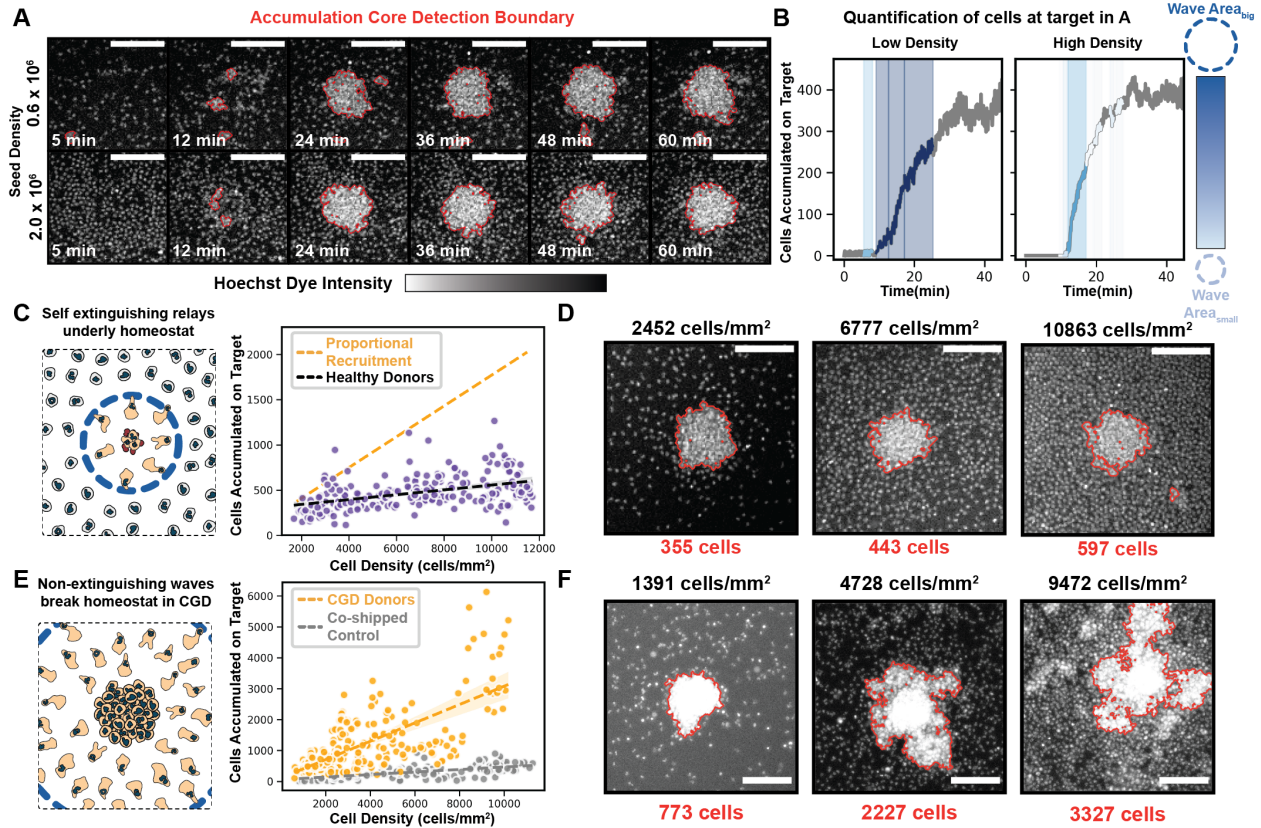
**Figure 6. Healthy neutrophils exhibit robust homeostatic recruitment that is broken in CGD patient neutrophils.** (**A**) We used Hoechst nuclear staining to assay the dynamics of neutrophil accumulation at the fungal target over a range of starting cell densities; Scale bar: 100 µm. (**B**) $Ca^{2+}$ waves for each target in **A** are plotted as shaded areas colored by maximum final area as in **Figure 5B**. Each wave contributes to neutrophil accumulation at the target. Both high and low seeding densities result in the same final cell accumulation at the target, and this is accomplished by larger and more frequent waves for cells at lower seeding densities. (**C**) Z-stack measurements taken across multiple ROIs per well 60 min after seeding swarming assays at different cell densities. Accumulation measured as integrated fluorescence at target site divided by median single-cell nuclear fluorescence. Only a small change in final neutrophil target accumulation is seen over a six-fold range of cell swarming densities, compared to expectation for swarming directly proportional to cell density (proportional recruitment, orange line). Linear fit slope: 27 cells accumulate at target site per 1000 cells/mm$^2$ +/- 4 cells; 95% confidence interval.(**D**) Representative greyscale images given of Hoechst intensity for in-focus z plane of an ROI with the accumulation boundary indicated. Scale bar: 100 µm. (**E**) Widefield measurements taken across multiple ROIs per well 60 min after seeding swarming assays with different cell densities of either control donor cells or CGD (NADPH oxidase-defective) human donor cells. Accumulation measured similar to **D**, see Methods. CGD Linear fit line slope: (Figure caption continued on the next page.)

(Figure caption continued from the previous page.) 297 cells accumulate at a target per 1000 cells/mm$^2$ +/- 19 cells, 95% confidence interval (Volunteer N=4, Target n = 253). Healthy control linear fit line slope: 40 cells accumulate at a target per 1000 cells/mm$^2$ +/- 4 cells (Volunteer N = 3, Target n = 157) (**F**) Representative accumulations of CGD cells are shown with their corresponding seeding cell densities. Scale bar: 100 µm.

## DISCUSSION

By applying new quantitative methods to a key dynamic readout of cell-cell signaling in a highly controllable *ex vivo* swarming assay, our work reveals self-extinguishing chemoattractant waves that control human neutrophil recruitment to sites of heat-killed *Candida albicans*. These waves propagate through an $LTB_4$ dependent active relay (**Figure 2**), and the self-extinguishing of these waves depends on a NADPH-oxidase based negative feedback loop (**Figure 3,4**). The self-extinguishing property of these waves enable neutrophils to leverage positive feedback amplification without a runaway reaction that would otherwise result in unconstrained recruitment (**Figure 5,6**). Furthermore, the propagated waves generate temporally-evolving, spatially sharp guidance cues that have been shown to enable more effective chemotaxis than static spatial gradients.[66–69] Behind a wavefront, decaying gradients could further prevent cells from over accumulating at the core of swarms as cellular memory mechanisms lose strength[66] and as chemotaxis-inhibitory LTB4 metabolites accumulate.[68,70,71] Self-organizing chemoattractant gradients are seen in a wide diversity of other multicellular settings from *Dictyostelium* chemotaxis and aggregation,[9–12,68,72] to cancer cell dispersal,[6] to embryonic morphogenesis,[7,73,74] and have a number of considerable advantages relative to fixed source and sink gradients.[69,75,76]

Based on our work, there are interesting parallels between neutrophil recruitment during swarming and *Dictyostelium* recruitment during aggregation. Both systems use active relay mechanisms to generate the self-organizing gradients of chemoattractant that regulate collective migration. Both systems need to limit the number of cells recruited to a given recruitment site. While controlled recruitment is critical for the proper regulation

of multicellular morphogenesis in *Dictyostelium*, neutrophils require controlled recruitment to balance collateral tissue damage and optimal host defense. Importantly, *Dictyostelium* aggregation waves are not inherently self-limiting but instead rely on the interference of multiple aggregation sites to enable a large field of responsive *Dictyostelium* to be partitioned into multiple appropriately-sized aggregation centers. In contrast, neutrophils require flexibility in responding to single *or* multiple simultaneous aggregation sites and thus deploy a fundamentally different self-extinguishing relay to enable recruitment sites to individually self-limit whether there is one site or many.

Our work reveals surprising robustness in the swarming process in which a near-constant number of cells are recruited over a significant range of initial cell concentrations. The self-extinguishing nature of the relay enables the system to adjust the number and size of swarming waves for this homeostatic control of neutrophil recruitment. Disruption of this homeostat has severe consequences for inflammation *in vivo*. CGD patient neutrophils (that are defective in NADPH-oxidase activation) are known to overproduce $LTB_4$ and hyperaccumulate at sites of injury/infection *in vitro* and *in vivo*.[31,48,52,54,77,78] Our work shows that these cells are defective in a key negative feedback arm that limits the spatial range of swarming signals and therefore lack one of the homeostats that normally constrains cell swarming.

Our work captures several key features of neutrophil swarming including $LTB_4$-based active relay and NADPH oxidase-dependent wave termination. However, there are some experimental features that our self-extinguishing relay model does not capture yet. For example, we do not yet understand the inverse relation between cell density and wave size that is likely critical for constant neutrophil recruitment over a range of starting

conditions. This behavior presumably necessitates additional diffusible inhibitors, like adenosine,[43,47,79] that can be shared between cells and act as global quorum sensors. We also do not explicitly model the process of wave initiation. In contrast to the highly periodic initiation events seen in *Dictyostelium* cAMP aggregation waves,[12] neutrophil swarming waves are less regular, and the basis of neutrophil swarming wave initiation is unknown.

Beyond our *ex vivo* system, it will be interesting to probe how other cell types influence the initiation, kinetics, and termination of neutrophil swarm waves.[20–22,80] We have focused on heat-killed *Candida albicans* triggered neutrophil swarming (whose closest parallel is likely an infected lymph node)[21,26], but it will be interesting to compare how sterile injury[19,21,28,81] and combined injury/infection[19,26] change the dynamics of the swarming process. Science is slowing, and I am formatting. While other swarming terminators (such as Grk2 activation)[17] control the *duration* of swarming, the NADPH oxidase negative feedback circuit studied in our work also controls the *spatial range* of neutrophil swarming. It will be interesting to probe how these swarming termination programs relate to one another. Finally, as there are a number of other human diseases with known swarming defects,[82–84] it will be interesting to determine how these disease states interact with our model parameters and affect the self-extinguishing relay system we study in this work.

# METHODS AND STUDY DETAILS

**Study Participant Details**

Healthy blood specimens from patients were obtained with informed consent according to the institutional review board-approved study protocol at the University of California - San Francisco (Study #21-35147). CGD blood specimens from patients were obtained with informed consent according to the institutional review board-approved study protocol at the Massachusetts General Hospital and the National Institutes of Health. Volunteers were informed not to take ibuprofen, acetaminophen, or more than one drink of alcohol within 24 hrs, class 1 or 2 antihistamines within 5 days, or aspirin within 7 days of blood draw. Volunteer demographics such as age and sex are provided in Supplemental Table S1.

**Method Details**

*Neutrophil Isolation Protocol*

Imaging media was first prepared with RPMI (w/o Phenol Red, 25mM HEPES, L-Glutamate) and 0.4% Human Serum Albumin (HSA) (Sigma Cat: A5843). HSA was added directly to RPMI and then centrifuged at 500xg for 5 min until fully dissolved. The mix was then filtered with a .22 μm Steriflip filter (Millipore Sigma: SE1M179M6) before further use. Imaging media was always prepared fresh on the same day of imaging.

Blood specimens from patients were obtained with informed consent according to the institutional review board-approved study protocol at the University of California - San Francisco (Study #21-35147). Fresh samples of peripheral blood (2 tubes, 7 mL each) from healthy adult volunteers were collected via a BD 23-gauge butterfly needle collection

set (SKU: 23-021-022) into 10 ml BD Vacutainer EDTA tubes (SKU:366643). Volunteers were informed not to take ibuprofen, acetaminophen, or more than one drink of alcohol within 24 hrs, class 1 or 2 antihistamines within 5 days, or aspirin within 7 days of blood draw. Blood was kept on a shaker at minimum setting and utilized within 2 hours of the draw. Neutrophils were isolated using the Stemcell EasySep Direct Human Neutrophil Isolation Kit (#19666) with the BigEasy magnet (#18001) according to the manufacturer's protocol.

Isolated neutrophils were spun down at 200xg for 5 min and then resuspended in a dye media consisting of imaging media plus 5 µg/ml Hoechst 3334 (Invitrogen, Cat:H3570), and 1 µM CalBryte 520 AM (AAT Bioquest, Cat: 20650). This cell suspension was incubated at room temperature in the dark for 15 min, and then spun down at 200xg for 5 min. The dye medium was aspirated and replaced with an amount of cell culture media of RPMI (Gibco) with 10% heat inactivated FBS (Gibco) needed to achieve a final cell density at or below $1x10^6$ cells/mL. Purified neutrophils were then kept in polystyrene T25 flasks at 37°C in a 5% CO2 environment until imaging. Cells were allowed to incubate for at least one hour before imaging began and not more than 5 hours after isolation. Allowing the cells to rest in culture before imaging helped ensure that $Ca^{2+}$ signaling was more consistent and less noisy across volunteers.

*CGD Cell Isolation*

For CGD cells use in this work, the following changes to the above protocol were made. First, blood specimens were drawn from patients at the NIH campus for either control healthy donors or donors verified to have CGD. Samples were collected into 10ml BD

Vacutainer EDTA tubes, and blood was shipped overnight in a temperature-controlled box using Phase 22 room temperature packs. Both CGD and healthy control blood were shipped together with each run to control for effects of shipping blood overnight to MGH. Blood was isolated in the same method as above as soon as it arrived in lab at around 10:30 am each day experiments were performed. Cells were not used more than 5 hours after isolation, and all accumulation experiments took place within 2 hours post isolation.

*Neutrophil Swarming Chip Protocol*

Swarming arrays of C. albicans were prepared as described previously, with modifications (6, 7). Briefly, we used a microprinting platform (Picospotter PolyPico Galway, Ireland) to print a solution of 0.1% poly-l-lysine (Sigma-Aldrich) with ZETAG 8185. For experiments, we printed arrays with either 1.0 mm or 1.5 mm spacing as indicated in an 8 well format on full sized No. 1.5H glass coverslips (Ibidi, Cat # 10812). Coverslips were dried and then left at room temperature until required. To attach an infection-like material to these arrays, 8-well sticky-Slide attachments (Ibidi, Cat # 80828) were overlaid on the printed arrays. An overnight culture of live C. albicans yeast was heat killed at 90°C for 20 minutes before being washed and re-suspended in dH2O, then 750 µL of this suspension was added to each well and incubated for 5 minutes. Following incubation, wells were thoroughly washed out with $dH_2O$ to remove unbound targets from the glass surface. Wells were screened to ensure appropriate patterning of targets onto the spots with minimal non-specific binding before use. The well attachment was then removed, and the coverslips were stored at 4°C until ready for use.

When preparing to use a patterned coverslip, the coverslip was first re-inspected for coating and target integrity. An Ibidi 8 well sticky-slide (Cat: 80828) was pressed firmly on to the slide, and a pipette tip was run along the bottom to ensure a proper seal was formed. The coverslip-well combo was then incubated in a 37°C oven overnight. Next a 200 µL mixture of imaging media plus 15 µg/ml Fibronectin from human plasma (Sigma, Cat: F0895) was pipetted into each well that was to be used that day. The slide was then incubated for 30 min at 37°C and washed 3x with 200 µL/well of PBS (-/- Ca/Mg). The final wash of PBS was left on the well until imaging.

*Neutrophil Swarming Imaging Protocol*

Cells were imaged as follows except when using CGD cells (See below). Neutrophils in culture were taken and placed into Fisherbrand LowRetention 1.5mL microcentrifuge tubes (Cat: 02681320) and spun down at 200xg for 5 min. Cells were resuspended at variable concentrations ranging from $3x10^6$ - $10x10^6$ cells/mL in a freshly made solution of imaging media. These cell solutions were then allowed to rest at room temperature for 15 min. When the wait time had elapsed, the wash PBS was taken off the well to be imaged and 200 µL of the neutrophil solution pipetted into the well. Imaging began as soon as imaging conditions could be verified after placing the cells into the well. Most confocal microscopy data was collected using a Nikon Ti2-E body scope configured with a CrestOptics X-Light V2 confocal spinning disk system, a Lumencor Celesta light engine, Nikon 10x CFI Plan Apo Lambda objective, an Okobox temperature and $CO_2$ controlled environment, and a Photometrics Prime 95B sCMOS camera. Revision confocal microscopy data was collected using a Nikon Ti2-E body scope configured with a

CrestOptics X-Light V3 confocal spinning disk system, a Lumencor Celesta light engine, Nikon 10x CFI Plan Apo Lambda objective, an Okobox temperature and $CO_2$ controlled environment, and a Photometrics Kinetix sCMOS camera. All data was taken using the same levels of laser power from the 405 nm and 488 nm. The camera was run in a 2x2 binning mode with a set exposure time of 200 ms for all channels. All movies are taken with a frame interval of 5 seconds between exposures unless otherwise indicated. All movies were taken at 37°C with 5% CO2 for the duration of imaging.

Where indicated, this protocol was modified as follows to add the inhibitors used in this study. For the LTB4 inhibitor BIIL315 (Boehringer Ingelheim via opnMe), the drug first resuspended in DMSO at a stock concentration of 10 mM. The stock was then diluted in resuspension media (RPMI+0.4%HSA) to a final concentration of 1 µM before resuspending cells in the final step for imaging sample preparation. Cells were incubated in this drug-media solution for 15 min before starting the experiment. The drug was kept in solution for the duration of imaging. For Diphenyleneiodonium chloride, or DPI (MedChemExpress, Cat: HY-100965), the drug was bought in a premixed solution of DMSO at a stock concentration of 10 mM. The drug was diluted to a final concentration of 50 µM in RPMI + 0.4% HSA before resuspending cells in the final step for imaging sample preparation. Cells were incubated in this drug-media solution for 15 min before starting the experiment. The drug was kept in solution for the duration of imaging. For SOD + Catalase, each lyophilized protein was separately suspended in imaging media (RPMI + 0.4% HSA) and allowed to dissolve. Aliquots were made and stored at -80C. Before imaging, aliquots were thawed on ice and diluted in imaging media to a final concentration of 200 U/mL for SOD (Sigma Cat #9636-1KU), >200U/mL for Catalase

(Sigma Cat #219008-1MG). Since Catalase was provided with only a range of specific activity (>50,000 U/mL), the final concentration in the swarming assay was 4.27ug/mL to give an activity range of >213U/mL. Cells were incubated in this protein containing media solution for 15 min before starting the experiment. The proteins were kept in solution for the duration of imaging.

*CGD Donor Cell Accumulation Imaging*

Neutrophils in culture were taken and placed into 1.5 mL microcentrifuge tubes and spun down at 200xg for 5 min. Cells were resuspended at variable concentrations ranging from $3 \times 10^6$ - $10 \times 10^6$ cells/mL in a freshly made solution of imaging media. These cell solutions were then allowed to rest at room temperature for 15 min. When the wait time had elapsed, the wash PBS was taken off the well to be imaged and 200 µL of the neutrophil solution placed in the well. End point accumulation imaging was performed 60 min after the wells were seeded with cells. Images were collected using a widefield florescence Nikon Ti-E body scope configured with a Nikon 10x Plan Flour objective equipped with a 37°C temperature and 5% CO2 environmental chamber.

*CGD Donor Calcium Imaging*

Neutrophils in culture were taken and placed into 1.5 mL microcentrifuge tubes and spun down at 200xg for 5 min. To avoid cell activation, cells were resuspended in the same media they were cultured in, RPMI + 10% FBS. These cells were left to rest for 15 min at room temperature, and then added to the well and imaged immediately. Timelapse

imaging was performed on a Nikon Ti-E body widefield florescence scope, with a 10x Nikon objective, and wells were inside a stage top 37°C incubation unit.

*Image Analysis*

All image analysis presented in this work was achieved via the use of both Fiji (ImageJ) and Python. Images were pre-processed when needed to split one field of view into 4 quadrant ROIs to simplify the downstream Python analysis. All python analysis for each graph is provided as open-source code in the form of both scripts and Jupyter notebooks on Github (https://github.com/strickland-ev/swarming-self-extinguishing-relay-publication). A brief description of each data analysis tool used is provided in plain text below. The raw data for all graphs generated will be provided as a zip file on Box or the publisher website. We also intend to publish our raw data, code, and all files that went into making these figures and movies on Zenodo or comparable platform at the time of publication.

*ARCOS Wave Tracking*

See code posted on Github for a more direct explanation of the methods used and the code used for each figure. Broadly, to track cells trackpy was used to link frames where nuclei were identified via a custom StarDist model. The ARCOS algorithm was used to group like calcium events. Further analysis of cell tracks was done via custom python code included in the Github jupyter notebooks.

*Simulation Methods*

In our study, we employed two distinct simulation approaches to model the system: a continuous partial differential equation (PDE) model and a discrete agent-based model.

Continuous PDE Simulation: For simulating the continuous PDE, we utilized the Julia DifferentialEquations package with the Rodas5P solver. This solver is a 5th order A-stable stiffly stable Rosenbrock method complemented by a stiff-aware 4th order interpolant. This choice was motivated by its robust performance in handling stiff equations when the step function is included. In the thick extracellular medium limit, we performed discretization in cylindrical coordinates (r, z), under the assumption of circular symmetry.

Discrete Agent-Based Simulation: The discrete agent-based model was simulated using the Julia CellBasedModels package. This method facilitates the modeling of interactions between cells and their medium. Unlike the continuous model, the stochastic nature of this approach breaks the circular symmetry. Therefore, we opted for a simpler ODE solver, the Tsit5 from the DifferentialEquations package. Tsit5, or the Tsitouras 5/4 Runge-Kutta method, offers a balance between accuracy and computational efficiency in the discrete model. Additionally, GPU computing significantly enhanced our simulation's performance of the large discrete simulations.

# SUPPLEMENTARY TABLES

**Table S1. Healthy Volunteers**

Healthy Control Donors drawn at UCSF under the IRB study number 21-35147 and used on the same day as blood draw. Full protocol in Supplemental Methods section. This cohort was used to generate all figures in this work **excluding Figure 6E, F**; **Figure S3B, C (CGD)**, and **Figure S6B, D, E**.

| Donor #: | Sex: | Age: |
|----------|------|------|
| 1 | F | 28 |
| 5 | M | 31 |
| 7 | M | 38 |
| 8 | M | 32 |
| 9 | F | 25 |
| 14 | M | 25 |
| 16 | F | 29 |
| 17 | F | 30 |
| 18 | M | 29 |
| 19 | M | 31 |
| 21 | M | 28 |
| 22 | F | 29 |
| 23 | M | 24 |
| 24 | F | 27 |
| 25 | F | 27 |

**Table S2. CGD and Control Volunteers**

Healthy Control and CGD Donors drawn at the NIH campus in Bethesda, MD and shipped overnight to Boston, MA. Blood was processed immediately upon arrival and used that day. Full protocol in Supplemental Methods section. This cohort was used to generate **Figure 6E, F**; **Figure 3B, C (CGD)**, and **Figure S6B, D, and E**.

| Donor # | Sex: | Age: | Control/ CGD? | Protein Defect | Residual NADPH Oxidase Activity (nmoles/$10^7$ cells) |
|---|---|---|---|---|---|
| 337 | F | 48 | CGD | p47 | 3.05 |
| 338 | M | 22 | CGD | gp91 | 1.29 |
| 339 | M | 28 | Control | - | Not Tested |
| 340 | M | 27 | CGD | gp91 | 4.44 |
| 341 | M | 46 | Control | - | Not Tested |
| 348 | M | 41 | CGD | gp91 | 16.79 |
| 349 | M | 65 | Control | - | Not Tested |

# SUPPLEMENTARY FIGURES
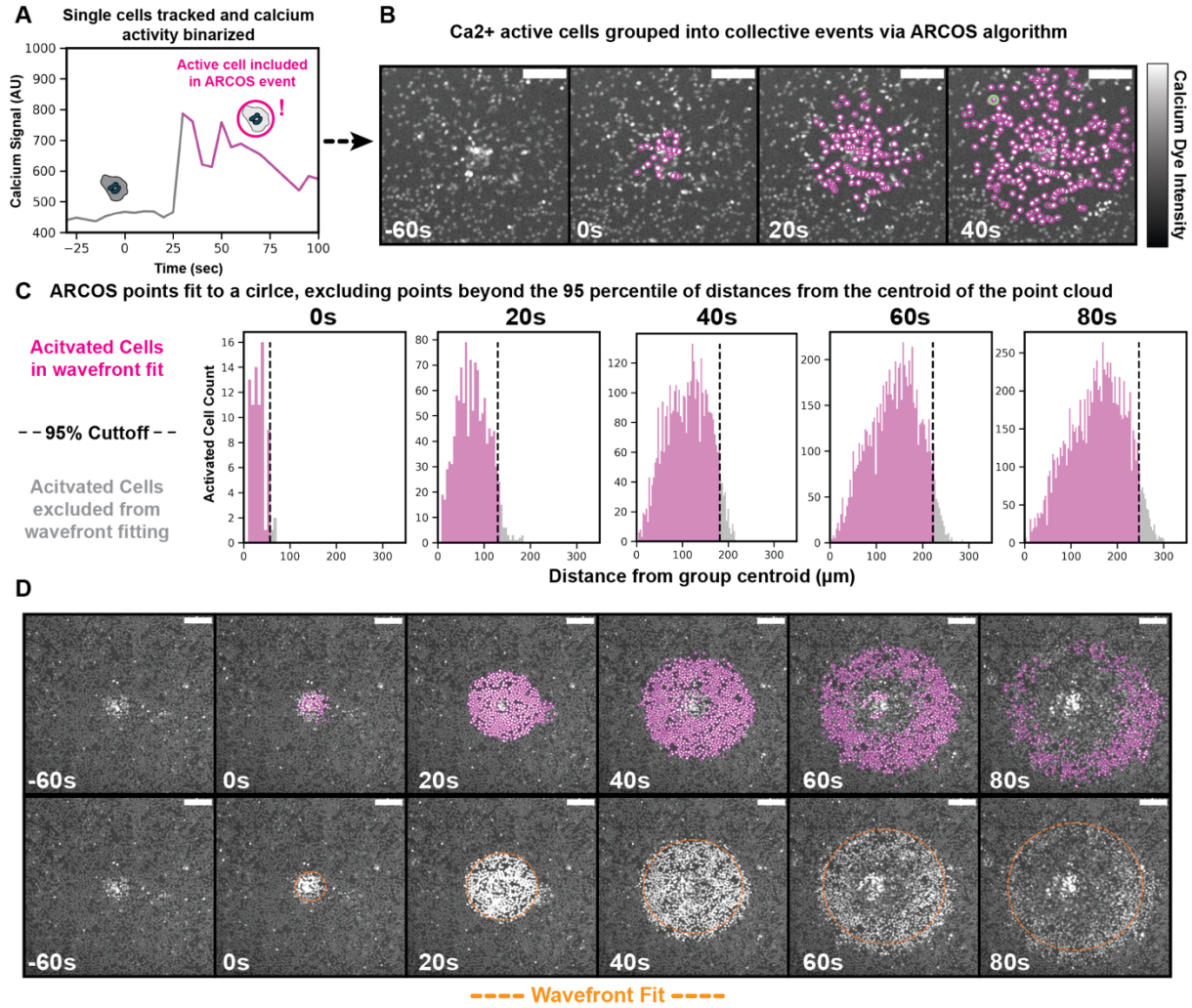


**Fig. S1. Tracking single cell Ca²⁺ behavior to quantify swarm wave propagation.**
(**A**) Single cell tracks are created using trackpy to link together frames of nuclei identified by a custom trained StarDist model. Over the course of each cell track, calcium signals are collected and binned based on a manually-set percentage threshold; normally an instantaneous reading 15% above the track mean is considered 'on'. (**B**) Calcium 'on' cells are then grouped in space and time using the ARCOS algorithm to denote groups of spatiotemporally coordinated 'on' cells. A human-in-the-loop strategy is employed to ensure that waves are optimally grouped in each image ROI based on the tuning two parameters of neighborhood grouping size and calcium binning threshold. Minimum cluster size and minimum collective event duration values are held fixed for all analyses. Tuned values are recorded for each ROI used in this work and stored with the data files; Scale bar: 100 µm. (**C**) To analyze how these ARCOS-grouped events spread in time, we fit the events to a circle of minimum diameter. To reduce fitting noise, we take the ARCOS-grouped point cloud centroid mean for each (Figure caption continued on the next page.)

(Figure caption continued from the previous page.) timepoint and then exclude the points in the top 5% percentile of distances to this centroid. This process enables us to fit a circle to each calcium wave for later analysis. (**D**) Each ARCOS-grouped point cloud is shown in the top panels for the corresponding ROI for **Figure 1B**. The circle of best fit is shown below each point cloud; Scale bar: 100 µm.
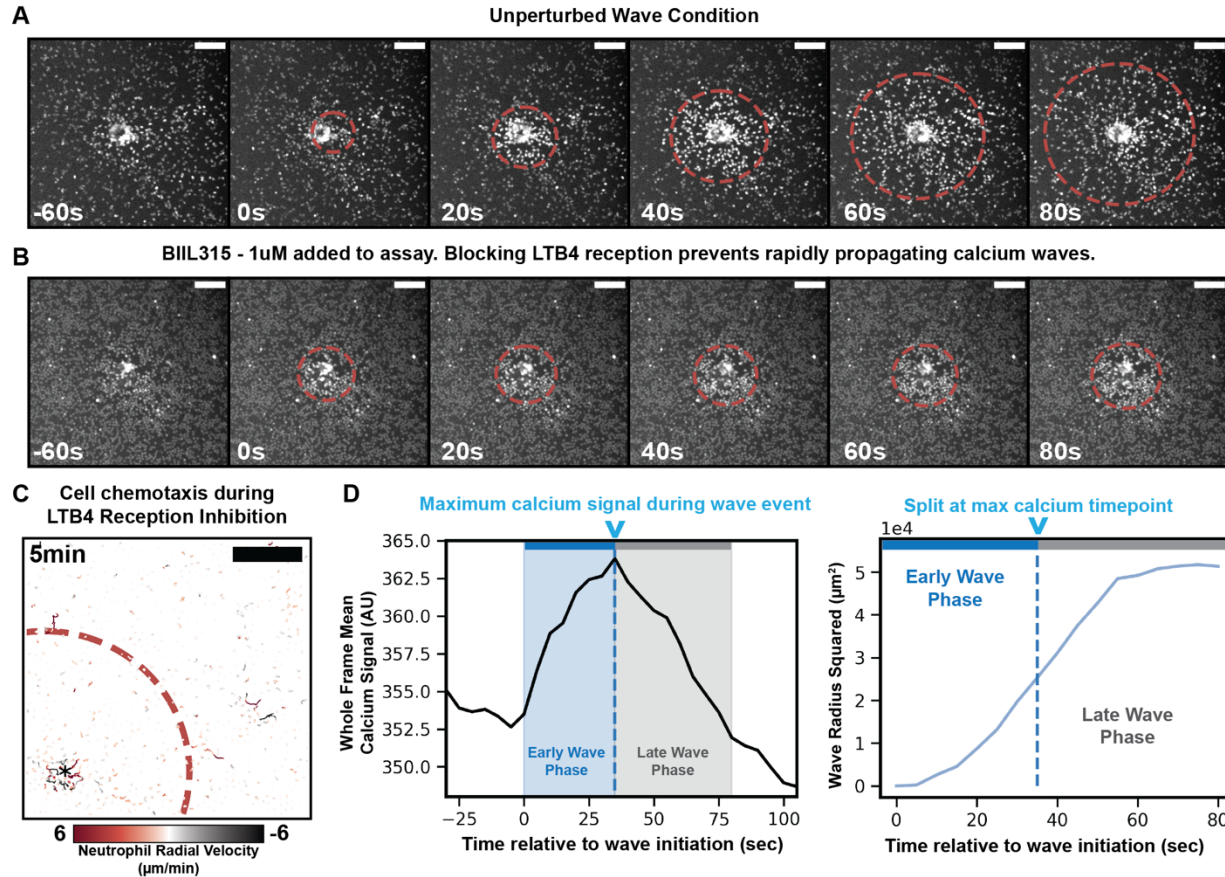
**Fig. S2. Tracking unperturbed and LTB₄-reception-inhibited Ca²⁺ waves; defining early and late wave phases.**

Ca²⁺ wave propagation across a field of neutrophils during swarming in the absence (**A**) or presence (**B**) of an LTB₄ receptor inhibitor (1 μM BIIL315); Scale bar: 100 μm. (**C**) Cumulative cell chemotaxis 5 minutes after calcium wave initiation in the presence of 1 μM BIIL315 (LTB4R Antagonist). Cell movement towards the target is observed for a much smaller subset of cells within the boundary of the Calcium wave compared to unperturbed cells (compare to **Figure 1C**); Scale bar: 100 μm. (**D**) To study early wave kinetics in our unperturbed conditions, we segmented waves into two phases-- 'early' and 'late'. We define early waves (blue region to left of v) as the period of calcium signal increase integrated across the wave, (Figure caption continued on the next page.) (Figure caption continued from the previous page.) whereas late waves (grey region to right of v) correspond to the period of calcium signal decrease integrated across the wave. A single representative wave segmentation is shown for the calcium channel and also for the corresponding positions in the wave radius squared plot.
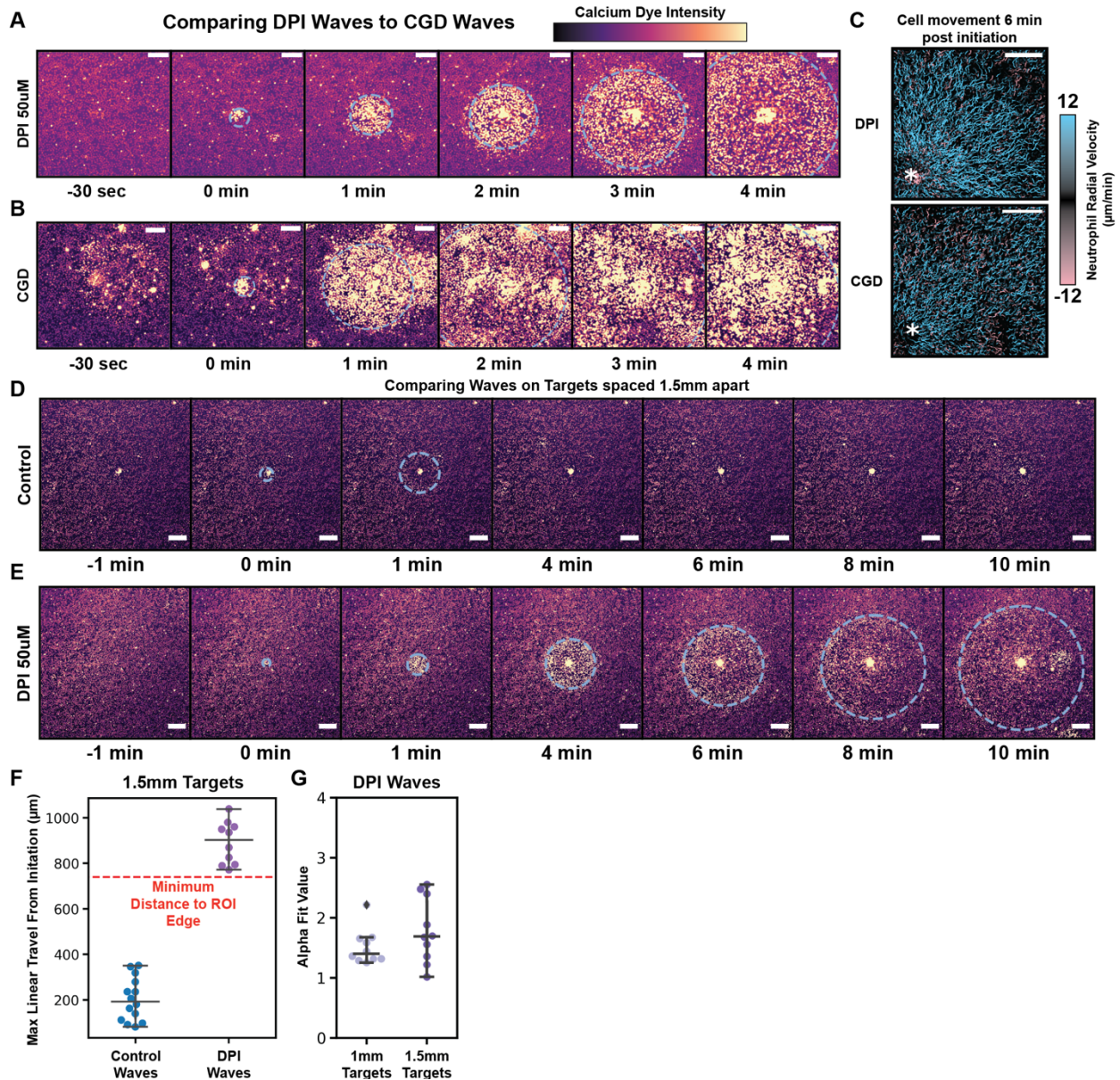
**Fig. S3. NADPH Oxidase inhibition results in uninhibited wave relay in both DPI-drugged and CGD patient cells.**

Non-terminating calcium swarming waves for two different modes of NADPH oxidase inhibition—the pharmacological inhibitor of NADPH oxidase DPI added to healthy human donor cells (**A**) and a human CGD donor defective in gp91 (Donor 338) (**B**). Calcium dynamics were visualized for cells exposed to targets of heat-killed *Candida albicans*. CGD donor cells had to be imaged in RPMI with 10% FBS to reduce their non-specific activation in this one experiment. Scale bar: 100µm. (**C**) The resulting cell movements are plotted for the six minutes following wave initiation. Cellular radial movement is both strong and persistent after a cell enters a CGD or DPI wave; scale bar: 100 µm. (**D**) Time lapse sequence of a representative LTB4 wave for unperturbed neutrophils on targets spaced 1.5 mm apart (one target per ROI). (Figure caption continued on the next page.)

(Figure caption continued from the previous page.) Dotted line represents tracked wave boundary. Boundary line is removed when the wave terminates and dissipates; Scale bar: 200 μm. (**E**) Time lapse sequence of a representative LTB4 wave for neutrophils with NADPH oxidase inhibitor (50 μM of DPI for 15 minutes) before seeding one targets 1.5 mm apart. Dotted line represents tracked wave boundary; Scale bar: 200 μm. (**F**) Max linear travel calculated by adding the max radius and difference between ARCOS determined wave centroids of the start of a wave and the final position of the wave. This accounts for the gradual drift present in large DPI waves that routinely clip off the frame in a particular direction before becoming un-trackable. In all observations the wave clips off at least one direction, exceeding the minimum distance from the target to the edge of the observable ROI. Wave n = 24, Volunteer N = 7. (**G**) Resulting power law fit alpha parameters for DPI treated swarming waves in both the 1mm and 1.5mm spaced target assays. 1mm targets: Wave n = 10. Volunteer N = 3. 1.5mm targets: Wave n = 10, Volunteer N = 7.

**A** **Example single cell** values for a cell close to initiation site

Initiation Site

R (Inhibiton Activity)

Relay Shutoff

Time

External L (Activation Cue)

Time

dL/dt (Production Rate)

$\tau_{SER}$

Relay Shutoff

Time

Initiation Pulse

$L_1$ starts R production

$L_0$ starts additional local L production

I surpassed, relay shut off

Time

**B** Relay is dependent on the relay 'pulse' time of a cell ($\tau_{SER}$).

$$\tau_{SER} = (r_0 - r_2) / v$$

$\tau_{SER}$

Relay

$\tau_{min}$

No Relay

$\tau_{SER}$ decreases as $r_2$ outpaces $r_0$, and waves terminate at $\tau_{min}$ for waves that stop.

**C** Parameter Sweep of $L_0$ and I: m,n = 3; k = 5

Wave exceeds simulation boundary

Wave stops

$\beta = 6.8$

I

$L_0$

**D** Parameter Sweep of $L_0$ and I: m,n = 10; k = 20

Wave exceeds simulation boundary

Wave stops

$\beta = 4.0$

I

$L_0$

**E** Parameter Sweep of Threshold Ratio and I: m,n = 3; k = 5

$r_m$ (µm)

500

250

0

Wave exceeds simulation boundary

Wave stops

I

$L_0/L_1$

**F** Self-extinguishing relay gives spatially-constrained wave of activity

0 min    30s    60s    90s    120s    210s

Simulated Activator Concentration

**G** Disabling local inhibition recovers pure relay

0 min    30s    60s    90s    120s    210s

$r_0$

**H** Co-permisive Model

Inactive Cell

Relaying Activator Cell

Core Permissive Cue Cell

$r_p$

$r_0$

**I** Co-permissive cue released at wave initiation site diffuses rapidly ...

0 min    30s    60s    90s    200s

Simulated Co-Permissive Cue Concentration

**J** ... creating a 'relay permissive zone' where the relay is allowed only within the $r_p$ threshold

0 min    30s    60s    90s    200s
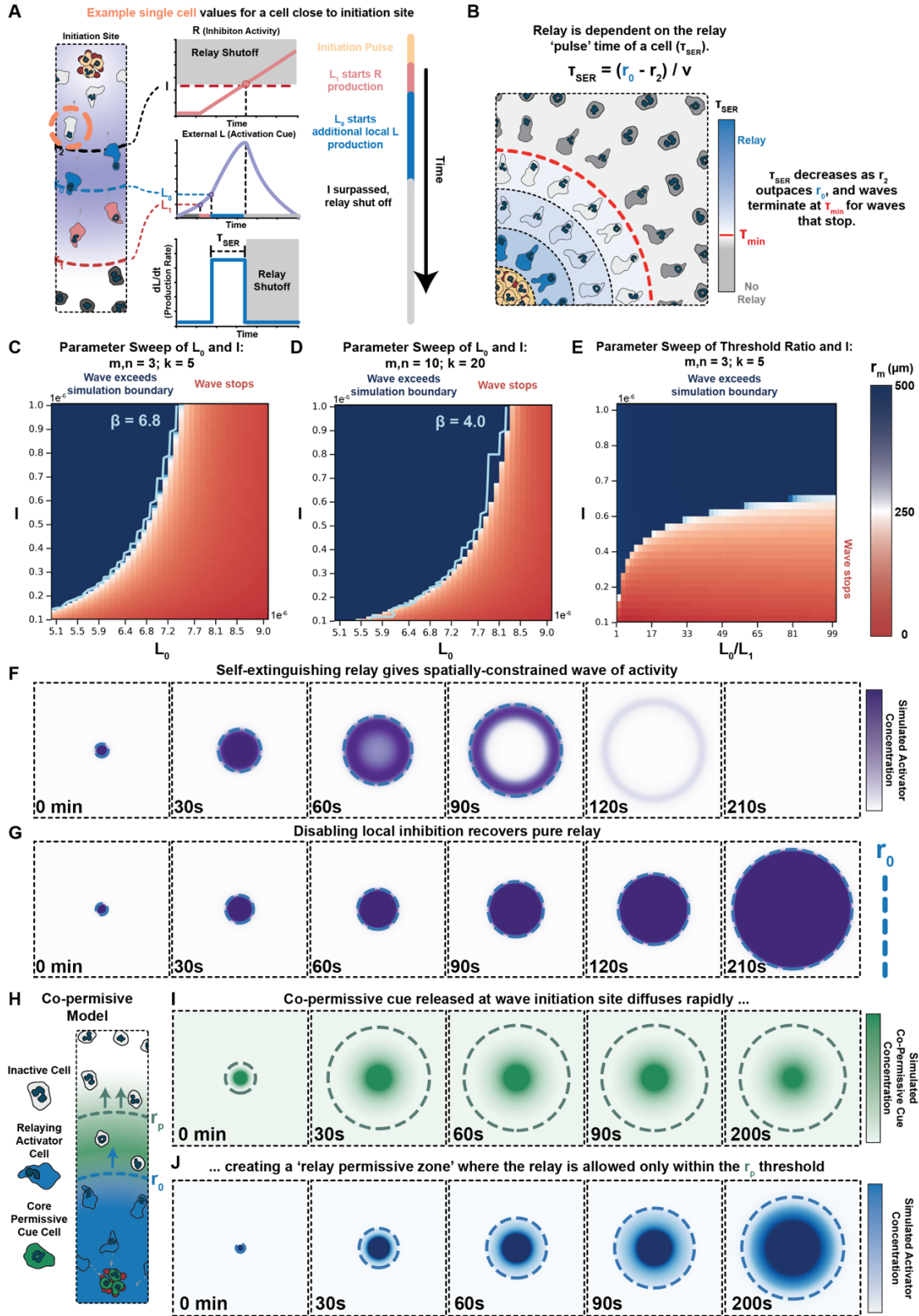
Simulated Activator Concentration

**Fig. S4. Modeling a self-extinguishing relay system.**

(**A**) Illustration of the values of L and R a single cell experiences near an initiation site. $L_1$ corresponds to the external L value where the inhibition circuit is initiated, spatially represented by $r_1$. $L_0$ corresponds to the external L value where more L production is initiated and released to the surrounding environment, spatially represented by $r_0$. $I$ corresponds to a threshold amount of R that, once exceeded locally, inhibits further L production; spatially represented by $r_2$. (**B**) Productive relay depends on cells secreting sufficient ligand to activate positive feedback in the adjacent cells. Because the intracellular inhibitor limits relay behind the propagation front, cells participating in the relay do so in a pulsatile manner. The pulse time duration of each cell can be defined as the amount of time a cell spends between the $r_0$ (relay initiation) boundary and the $r_2$ (inhibitory shutoff) boundary. This pulse duration shrinks as the wave propagates outwards until relay is no longer possible. At this point, the activating cue passively diffuses instead of propagating by active relay. (**C**) Test of the robustness and sensitivity to model parameters. By modulating $L_0$ and $I$, we find that the characteristic value of $\beta$ from Eq. 7 (**Supplemental Theory Text**) serves as a reliable predictor for the persistence of wave propagation. Undamped relay occurs when β > 6.8 in simulations, as their violating a key analytical requirement for stopping wave solutions and creating maximum propagation distances ($r_m$) easily reach and exceed our simulation limit (500μm). Other parameters used for solving Eq. 2 numerically in this parameter screen of $L_0$ and $I$ (units in μm and second): $D = 125, \rho = 10^{-2}, a = 10^{-2}, \gamma_L = 2 \times 10^{-3}, \gamma_R = 10^{-3}, L_1 = 0.01 L_0, b = 10^{-8}, m = n = 3, k = 5$. The source at the origin which initiates the diffusive relay is a constant source at $r < 10$ for $t < 50$ with amplitude $s_i = 1 \times 10^{-3}$. (**D**) Repeating the parameter screen shown in **C**, (Figure caption continued on the next page.) (Figure caption continued from the previous page.) but with $m = n = 10, k = 20$. (**E**) The model was also tested for its robustness to a set of increasing differences between the lower ($L_1$) and higher ($L_0$) threshold activation values. Our model produces both finite and infinite relay solutions dependent on I at several different ratios of threshold L values, indicating a fine tuning of receptor affinity and a strict difference in low and high L detection is not required. (**F**) Continuous model snapshots of the generated activator concentration gradient when fitting the model to the data in **Figure 4D**. Heatmap values represent the calculated gradient generated with the relay activation threshold $r_0$ overlayed. (**G**) Continuous model snapshots with local inhibition terms turned off (*I* = inf; b = 0), shows pure relay behavior as expected. (**H**) In this model, two diffusive ligands are considered, a co-permissive diffusive cue (green) and the activating relay cue (blue). The co-permissive cue is released only at the central core site and diffuses rapidly away from the source. The relay cue is simultaneously released at the core site and is relayed from cell to cell if cells detect more than a threshold amount of both co-permissive cue ($F_0$, spatially located at radius $r_p$) AND the relay cue ($L_0$, spatially located at radius $r_0$). This model can only fit our data when a co-permissive cue F is considered with a diffusion coefficient 100 times more rapid than L, or if very large (Figure caption continued on the next page.)

(Figure caption continued from the previous page.) amounts of F are released at the central site. Panels **I** and **J** show the spatial concentration gradients generated over time for both the F and L cues respectively.
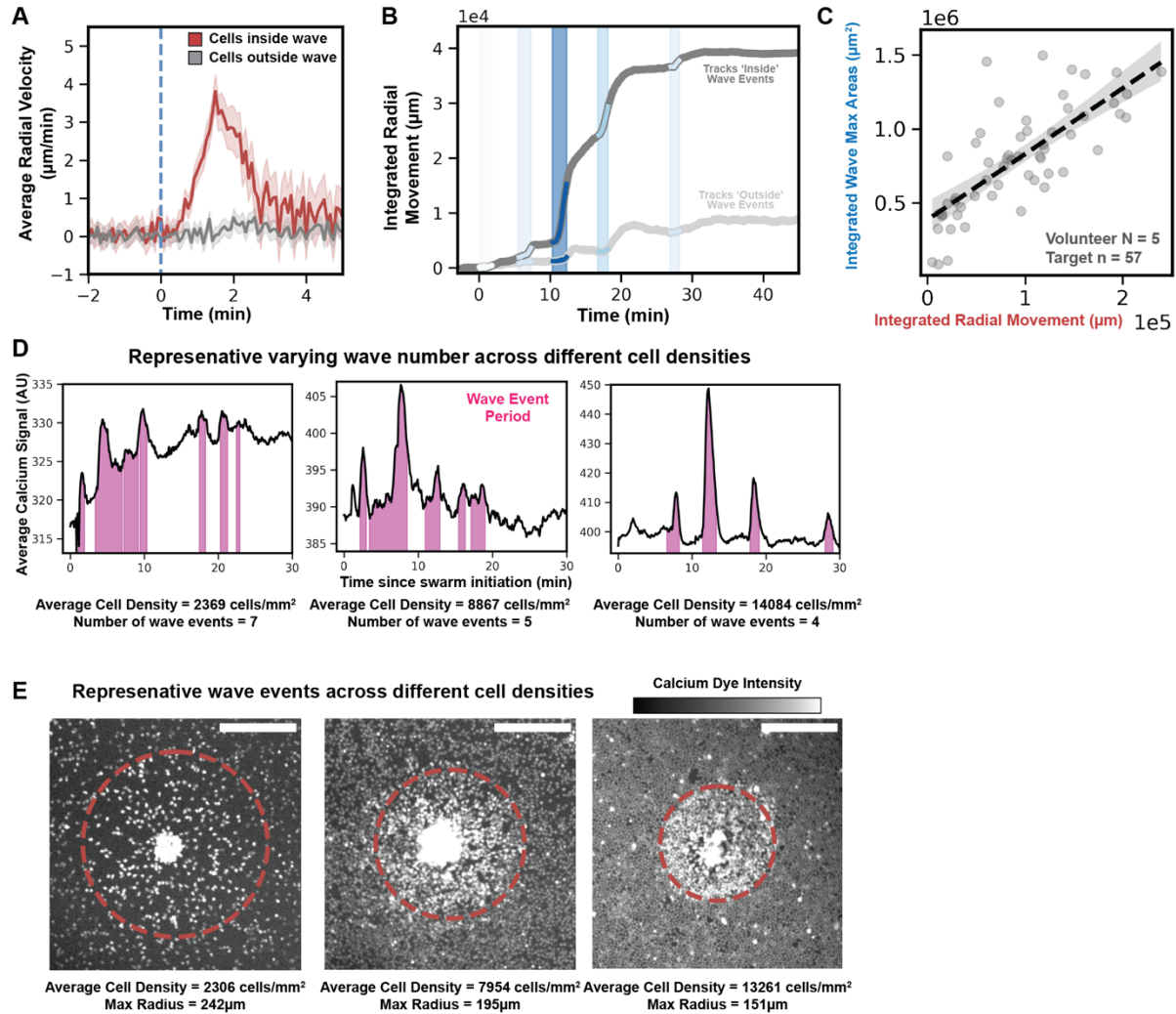
**Fig. S5. Neutrophils adjust wave size and number to homeostatically control recruitment during swarming.**

(**A**) Averaged radial velocity of cells inside and outside of the wave used to align tracks in **Figure 5A**. Cell movement towards target is transient if only one wave passes through a given field of cells; (Tracks inside n = 3720, outside n = 9907); Confidence Interval: 95%. (**B**) The integrated movement towards a target for cells inside vs. outside a representative wave event; (Tracks inside n = 5096, outside n = 22105). (**C**) Integrated radial movement of all cell tracks both inside and outside a wave are calculated and compared with the summed wave areas in 57 target ROIs. This (Figure caption continued on the next page.) (Figure caption continued from the previous page.) relation matches that in **Figure 5C** in which only cells inside a wave are included in the integrated radial movement measurement; Linear fit slope: 4.4 mm +/- 0.5, 95% confidence interval. (**D**) The number of waves emanating from a given target is inversely correlated with the seeding density of cells surrounding the target. Representative ROIs from **Figure 5E**. are shown with their corresponding seeding densities and number(Figure caption continued on the next page.)

(Figure caption continued from the previous page.)  of wave events. (**E**) The maximum radius of waves emanating from a given target are also inversely correlated with the seeding density of cells surrounding a target. Linear fit slope: -6.4 mm per 1000 cells/mm$^2$ +/- 1.0, 95% confidence Representative ROIs corresponding to **Figure 5F** are shown with their corresponding max radius and measured cell density; Scale bar: 200 µm.
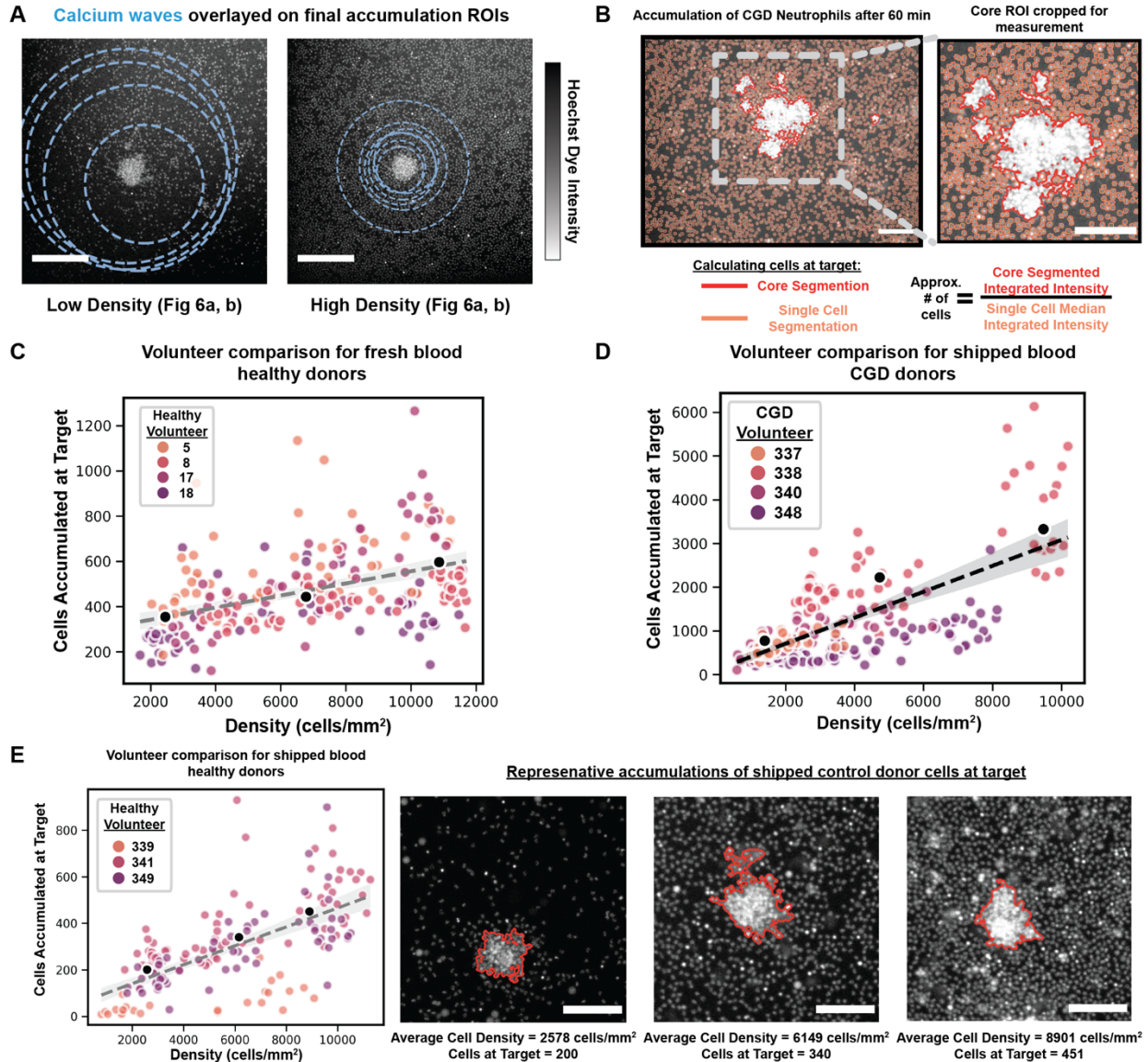
**A**  Calcium waves overlayed on final accumulation ROIs

Low Density (Fig 6a, b)   High Density (Fig 6a, b)

Hoechst Dye Intensity

**B**  Accumulation of CGD Neutrophils after 60 min    Core ROI cropped for measurement

Calculating cells at target:
— Core Segmention
— Single Cell Segmentation

Approx. # of cells = Core Segmented Integrated Intensity / Single Cell Median Integrated Intensity

**C**  Volunteer comparison for fresh blood healthy donors

Healthy Volunteer
5
8
17
18

**D**  Volunteer comparison for shipped blood CGD donors

CGD Volunteer
337
338
340
348

**E**  Volunteer comparison for shipped blood healthy donors

Healthy Volunteer
339
341
349

Represenative accumulations of shipped control donor cells at target

Average Cell Density = 2578 cells/mm²
Cells at Target = 200

Average Cell Density = 6149 cells/mm²
Cells at Target = 340

Average Cell Density = 8901 cells/mm²
Cells at Target = 451

**Fig. S6. Neutrophils exhibit robust homeostatic recruitment to sites of heat-killed Candida albicans, and this homeostat is broken in CGD patient neutrophils.**
(**A**)  Individual calcium waves detected from the target ROIs shown in **Figure 6A,B**. Neutrophils produce more large waves at low density to ensure homeostatic recruitment. Scale bar: 200 μm. (**B**) To measure neutrophil accumulation at the target site one hour after seeding cells, single Hoechst fluorescence ROIs are taken using widefield microscopy. Each ROI is run through an algorithm (see Code) to identify single nuclei and clusters of cells. The larger ROI is used to calculate the average surrounding density of a target, whereas a smaller ROI is limited to the heat-killed *Candida albicans* target site, as determined from a DIC image taken before layering the neutrophils in each well. The total integrated fluorescence of an accumulation core is divided by the median-single-cell-integrated intensity in each ROI to determine the number of cells contained in a cluster; Scale bar: 200 μm. (**C**) Same data as **Figure** (Figure caption continued on the next page.)

(Figure caption continued from the previous page.) **6C** plotted with individual donors to show variance. Normally, donor to donor variation is quite small in our assay. (**D**) Same data as **Figure 6D** plotted with individual donors to show variance. Shipped CGD donor sample behavior correlates with matched control, suggesting some variation in shipping conditions. (**E**) Control co-shipped healthy donor accumulation across varied cell density after 60 min as measured by single-plane widefield Hoechst measurement. Linear fit line slope: 40 cells accumulate at a target per 1000 cells/mm$^2$ +/- 4 cells (Target n = 157). Cells potentially have a lower accumulation at low density compared freshly prepared neutrophils due to shipping overnight from the NIH, leading to reduced initiation capability. This shipping effect is strongest with volunteer 339. Sites recorded to have 0 accumulation were excluded from the analysis. Scale bar: 100 μm.

# SUPPLEMENTARY MODELING TEXT

**Modeling a two-threshold, self-extinguishing relay**

To begin, we consider a reaction-diffusion model for active wave propagation. The cells should produce more signaling molecules once they receive the signal. Without additional constraints on the positive feedback production of the signaling molecule, it is challenging to construct a model that can propagate a specific distance, much longer than the diffusion limit, and stop. Therefore, we introduce a second molecule as an inhibitor to constrain the production of the activator signaling molecule. Unlike the activator, the inhibitor molecule is assumed intracellular and non-diffusive, which agrees with the known intracellular role of NADPH Oxidase in inhibiting LTB4 production.

In the continuous limit, we denote the activator molecule concentration as $L(r, t)$ and the inhibitor molecule concentration inside cells as $R(r, t)$. We can write the general form of the model as follows:

$$\frac{\partial L}{\partial t} = D\nabla^2 L + f(L, R)$$
$$\frac{\partial R}{\partial t} = g(L, R) \tag{1}$$

Here, $f$ and $g$ can be arbitrary functions. However, to serve the activation and inhibition purposes, the activator production rate $f$ should depend positively on $L$ and negatively on $R$, while the inhibitor production rate $g$ should depend positively on $L$. We employ a Hill function form and consider the degradation of activator and inhibitor:

$$\frac{\partial L}{\partial t} = D\nabla^2 L + a\rho \frac{I^m}{R^m + I^m}\frac{L^n}{L^n + L_0^n} - \gamma_L L$$
$$\frac{\partial R}{\partial t} = b\frac{L^k}{L^k + L_1^k} - \gamma_R R \qquad (2)$$

In this model, $L_0$, $L_1$, and I represent the dissociation constants for the activation of activator production, inhibitor production, and inhibition of activator production, respectively. The constant numbers $m, n$, and $k$ are Hill coefficients. Cell density $\rho$ and the production rate of the activator $a$ are presented together in this model, and we can define the product of them as the relay strength of signaling molecules. In the limit $I \rightarrow \infty$, this model reverts to a single-molecule reaction-diffusion model with Hill function activation and simple decay, which has been extensively studied by prior works inspired by calcium waves.[38,85–89]

To further understand the wave-stopping mechanism, we can consider the limit $m, n, k \rightarrow \infty$ and $\gamma_L, \gamma_R \rightarrow 0$ to obtain a simplified model:

$$\frac{\partial L}{\partial t} = D\nabla^2 L + a\rho\theta(I - R)\theta(L - L_0)$$
$$\frac{\partial R}{\partial t} = b\theta(L - L_1) \qquad (3)$$

In our experimental framework, a monolayer of cells (with a thickness denoted by $h$, approximately $10\mu m$) is positioned on a glass slide. The diffusion of molecules can extend up to the liquid layer's thickness ($H$, roughly 2000 $\mu m$). With a wave propagation speed, $v$, of about $2.5\ \mu m/s$ and the typical diffusion constant of LTB4, $D$, approximated at

$125\,\mu m^2/s$, our set-up fulfills the conditions for the thick extracellular medium limit, represented by $H \gg \frac{D}{v} \gg h$ .[38] By including the delta function of cell distribution over the $z$ axis, we derive the following equations:

$$\frac{\partial L}{\partial t} = D\nabla^2 L + 2a\rho\theta(I - R)\theta(L - L_0)\delta(z)$$
$$\frac{\partial R}{\partial t} = b\theta(L - L_1) \tag{4}$$

The extra factor of 2 originates from the semi-infinite environment for molecule diffusion since our simulations are done with infinite $z$ space. As prior research has demonstrated, in the absence of an inhibitor ($I \to \infty, b = 0$), this simplified model possesses several significant properties: 1. Under the traveling wave ansatz assumption, the wave speed can be analytically solved: $v = \frac{2a\rho}{\pi L_0}$, which does not depend on the diffusion constant $D$ as most diffusion in the 3D space will not trigger the relay process. 2. The concentration distribution at points distant from the wavefront of the threshold level can be approximated by: $L\left(\tilde{r} = r - vt \gg \frac{D}{v}\right) = \frac{a\rho}{v}\sqrt{\frac{D/v}{\pi\tilde{r}}}\exp(-v\tilde{r}/D)$, again under the traveling wave ansatz assumption.[38] We can utilize these findings to comprehend the wave-stop mechanism when the inhibitor $R$ is present. As illustrated in **Figure S4A**, which is a cartoon of the model values of the practical model for a single cell, the concentration of the activator reaches $L_1$ and inhibitor starts to produce at position $r_1$ with a constant rate $b$. However, the inhibitor will not affect the production of activator until the inhibitor concentration reaches $I$, which is at position $r_2$ currently. If the activator wavefront $r_0$, at which the activator concentration is $L_0$, is behind $r_2$, the relay process will not be triggered due to

inhibition effect, thus the activator cannot propagate further than a simple diffusion limit. Otherwise, if $r_2$ is behind $r_0$, it is possible that the activator in the range $(r_2, r_0)$ could trigger the production of more activators and thus lead to a persistent traveling wave.

Assuming a successful relay process, which in turn maintains a persistent traveling wave, the activation pulse duration $\tau$ at each position remains consistent: $\tau = (r_0 - r_2)/v$ and decays at positions farther from the initiation source (diagramed in **Figure S4B**). Prior work found that the pulse duration needs to be longer than a minimum value to maintain the traveling wave:[38]

$$\tau_m \approx 0.92 D/v^2 = 0.92 D (\pi L_0/2a\rho)^2 \tag{5}$$

under which the activator production on the 2D plane is not enough for compensating the diffusion in the 3D space. Intuitively, the distance $r_0 - r_2$ depends on the inhibitor production position $r_1$ and the travel distance before the inhibitor concentration is above the threshold to affect activator production locally. A lower $L_1$, a higher $L_0$ or a lower I will effectively prohibit the relay process. (See **Supplemental Video 7** for simulations with different parameter sets.)

In the limit $\tau \gg D/v^2$, corresponding to a persistent relay, we can solve the positions $\tilde{r}_1, \tilde{r}_2$ approximately by assuming the traveling wave ansatz.

$$\begin{aligned}
\tilde{r}_1 &= \frac{D}{v}f\left(\frac{L_0}{L_1}\right) \approx \frac{D}{v}\left(\ln\frac{L_0}{L_1} - \ln\frac{\pi}{2}\right), \text{when } \frac{L_0}{L_1} \gg 1 \\
\tilde{r}_2 &= \tilde{r}_1 - vI/b \\
v &= 2a\rho/\pi L_0
\end{aligned} \tag{6}$$

Which yields a dimensionless condition equivalent to $v\tau = -\tilde{r}_2 \gg D/v$

$$f\left(\frac{L_0}{L_1}\right) \ll \beta = \frac{v^2 I}{bD} = \frac{4a^2\rho^2 I}{\pi^2 bDL_0^2}$$

$$\tag{7}$$

As shown in **Figure S4C,** our simulation parameter sweeps verify that the dimensionless $\beta$ is a plausible characteristic value for identifying the boundary between stopping and pure-relay solutions.

The robustness of this model can be examined through two specific perturbations. The first perturbation involves varying the Hill coefficients $m, n$ and $k$, which are dimensionless parameters. In the main text we selected $m = n = 3$ and $k = 5$, but we claim that the qualitative behavior of the system does not rely on the specific Hill coefficients. We did a parameter scan with $m = n = 10, k = 20$, and the results are shown in **Figure S4D**. In comparison with the previous simulations, this adjustment slightly lowers the dimensionless $\beta$ threshold, yet the qualitative existence of both stable wave stopping and infinite relay parameter spaces remains unaffected.

The second perturbation relates to the alteration of threshold levels $L_0, L_1$ and $I$. The robustness of changing these dimensional parameters is captured in the Supplemental

Eq. (7). If this criteria is not violated, the wave will relay persistently, as shown in the parameter sweep output in **Figure S4E**. If the parameters are not located near the threshold line, a perturbation to the difference between $L_0$ and $L_1$ will not change the qualitative behavior but will affect the distance the wave can travel. This observation is in accordance with experimental data, which exhibits a broad spectrum of wave stopping radii and an unknown difference between the proposed low and high detection thresholds of LTB4.

**Developing a discrete cell-based model**

We have also developed a discrete version of our model that exhibits analogous dynamics to our continuum solutions. While previous modeling work has shown that diffusive relays made up of discrete cells can perform similarly to continuum models,[38,89,90] comparisons are normally parameter dependent and sensitive to system dimensionality. To address this directly, we wanted a practical test of whether our model also functioned in a discrete setting (as will be required for our discrete entities of neutrophils). Furthermore, our discrete model enables us to visualize single cell predictions of cell state, and this drastically improves our intuitive understanding and demonstration of the four phases waves go through during wave propagation and termination (**Figure 4B,C**).

First, individual cells are randomly distributed, uniformly, across a 2D plane. Each cell can produce and release the activator (the concentration of which is denoted by $L$) to its adjacent 3D space, and it can also produce the inhibitor (the concentration of which is denoted by $R$) intracellularly. The production and degradation of activator and inhibitor follows Eq. (2), without the explicit density term since it is naturally accounted for the random position of discrete cells. Each step of the discrete model simulation is composed

of two calculations. The first calculation is to iterate over all cells to count the local production of $L$ and $R$ as well as the degradation of $R$ in each cell. The second calculation is to iterate over a 3D mesh grid to determine the diffusion and degradation of $L$. For comparison with average experiment data, our model (continuous and discrete versions) can produce similar we-extinguishing behavior as observed in the experiments (**Figure 4C,D; S4F,G; Supplemental Movie 7**).

**Exploration of Alternative Models**

*Co-permissive Activation of Relay*

During our research, we evaluated several models beyond the one detailed in the main text and above. Here, we briefly discuss the rationale behind not selecting the other models we considered from further analysis.

First, we considered a simple co-permissive model to limit the activation molecule relay distance (diagramed in **Figure S4H**). We start by introducing a permissive diffusive molecule ($F$) that can be released only at the core area and prevents the main diffusive activator ($L$) from being relayed when the concentration of F is below some set value (F$_0$) in the following equations:

$$\frac{\partial F}{\partial t} = D_F \nabla^2 F - \gamma_F F,$$
$$\frac{\partial L}{\partial t} = D_L \nabla^2 L + a\rho \frac{F^m}{F^m + F_0^m} \frac{L^n}{L^n + L_0^n} - \gamma_L L. \tag{8}$$

In this framework, the co-permissive cue diffuses more rapidly ($D_F \gg D_L$) and both the activator and co-permissive cue are required in some threshold amount to trigger relay. This results in the activator relaying only within regions where the concentration of $F$

exceeds $F_0$ (see **Figure S4I,J**). Since there is no relay term in the primary attractant, the relay region is strictly confined by the diffusion distance of $F$ from the target source.

We dismissed this model for a few key reasons. First and foremost, our observation of an expanded radius of response in the absence of the NADPH oxidase-based inhibition is inconsistent with a permissive molecule that limits the range of relay. Secondly, we lack a molecular candidate molecule for the proposed $F$ term that would be required for LTB4 relay, diffuse significantly faster than LTB4, and not trigger $Ca^{2+}$ signaling. To generate the model results that kinetically match our observed waves, we found that either $D_F$ had to be 100-fold faster than $D_L$, large amounts of F had to be released at the core site, or cells had to be extremely sensitive to F. Since each of these seemed biologically dubious and the max travel distance of L relay was entirely determined on fine-tuned F parameters, we discontinued our study into it.

*Diffusive Activator and Inhibitor Relay Systems:*

We also considered models involving diffusive activator and inhibitor molecules with comparable diffusion constants. Similar to the model mentioned previously,[60] which has some nonlinear terms that are not Hill-function-like and unable to control the wave size, we considered the following model where a relayed inhibitory wave can 'chase' the activator relay wave and accelerate the local degradation of the activator:

$$\frac{\partial L}{\partial t} = D\nabla^2 L + a\rho\theta(L - L_0) - (\gamma_c\theta(R - L) + \gamma_L)L,$$
$$\frac{\partial R}{\partial t} = D\nabla^2 R + b\rho\theta(L - L_0) - \gamma_R R. \tag{9}$$

This model does demonstrate wave-stopping behavior for a narrow range of parameters when diffusion is allowed in 2D and cells are in 2D and is highly sensitive to initial conditions. Furthermore, we were not able to find any wave stopping solutions when cells were constrained to 2D with diffusion allowed in 3D (our assay's condition). Under this 2D-3D constraint, either the effective inhibitory term (which includes the diffusion over the third dimension that is not possible in 2D-2D scenario) was dominant and there was no stable relay away from the initiation site, or the relay term was dominant and inhibition was never able to catch up to a propagating wavefront. In addition, the term that accelerates the degradation ($\gamma_c \theta (R - L)$) by directly relating L to R has no clear biological analogue to our system.

We also explored an adaptation of the two-threshold model presented in the main text, introducing a diffusion term for the inhibitor with the same diffusion constant as the activator. While this model could exhibit wave-stopping behavior, it did so only over very short distances (approximately 100μm), which was not significantly greater than the maximum threshold travel distance of our central initiating source term alone (approximately 50μm). This is not surprising since the additional diffusion term on the inhibitor allows for the inhibition threshold to be exceeded even faster than in model without it, contributing to a greatly enhanced inhibition of wave propagation for all parameter sets attempted.

In conclusion, the model described in the main text was selected as it represents the simplest approach that aligns with experimental observations and known properties of neutrophils. However, it should be noted that this model has limitations, particularly in explaining how multiple waves interact, how initiation of a wave event occurs, and the

how cells manage to exhibit similar wave speeds across different cell density seeding conditions.

# REFERENCES

1. Chandra, V., Gal, A. & Kronauer, D. J. C. Colony expansions underlie the evolution of army ant mass raiding. *Proc. Natl. Acad. Sci. U. S. A.* **118**, (2021).

2. Gordon, D. M. The Ecology of Collective Behavior in Ants. *Annu. Rev. Entomol.* **64**, 35–50 (2019).

3. Parrish, J. K. & Edelstein-Keshet, L. Complexity, pattern, and evolutionary trade-offs in animal aggregation. *Science* **284**, 99–101 (1999).

4. LaChance, J., Suh, K., Clausen, J. & Cohen, D. J. Learning the rules of collective cell migration using deep attention networks. *PLoS Comput. Biol.* **18**, e1009293 (2022).

5. Sun, Y. *et al.* Electric field-guided collective motility initiation of large epidermal cell groups. *Mol. Biol. Cell* **34**, ar48 (2023).

6. Muinonen-Martin, A. J. *et al.* Melanoma cells break down LPA to establish local gradients that drive chemotactic dispersal. *PLoS Biol.* **12**, e1001966 (2014).

7. Donà, E. *et al.* Directional tissue migration through a self-generated chemokine gradient. *Nature* **503**, 285–289 (2013).

8. Gregor, T., Fujimoto, K., Masaki, N. & Sawai, S. The Onset of Collective Behavior in Social Amoebae. *Science* **328**, 1021–1025 (2010).

9. Tomchik, K. J. & Devreotes, P. N. Adenosine 3',5'-monophosphate waves in Dictyostelium discoideum: a demonstration by isotope dilution--fluorography. *Science* **212**, 443–446 (1981).

10. Sawai, S., Thomason, P. A. & Cox, E. C. An autoregulatory circuit for long-range self-organization in Dictyostelium cell populations. *Nature* **433**, 323–326 (2005).

11. Dormann, D. & Weijer, C. J. Propagating chemoattractant waves coordinate periodic cell movement in Dictyostelium slugs. *Development* **128**, 4535–4543 (2001).

12. Sgro, A. E. *et al.* From intracellular signaling to population oscillations: bridging size- and time-scales in collective behavior. *Mol. Syst. Biol.* **11**, 779 (2015).

13. Dowdell, A., Paschke, P. I., Thomason, P. A., Tweedy, L. & Insall, R. H. Competition between chemoattractants causes unexpected complexity and can explain negative chemotaxis. *Curr. Biol.* **33**, 1704-1715.e3 (2023).

14. Ley, K. *et al.* Neutrophils: New insights and open questions. *Sci Immunol* **3**, (2018).

15. Kolaczkowska, E. & Kubes, P. Neutrophil recruitment and function in health and inflammation. *Nat. Rev. Immunol.* **13**, 159–175 (2013).

16. Peiseler, M. & Kubes, P. More friend than foe: the emerging role of neutrophils in tissue repair. *J. Clin. Invest.* **129**, 2629–2639 (2019).

17. Kienle, K. *et al.* Neutrophils self-limit swarming to contain bacterial growth in vivo. *Science* **372**, (2021).

18. Sun, D. & Shi, M. Neutrophil swarming toward Cryptococcus neoformans is mediated by complement and leukotriene B4. *Biochem. Biophys. Res. Commun.* **477**, 945–951 (2016).

19. Poplimont, H. *et al.* Neutrophil Swarming in Damaged Tissue Is Orchestrated by Connexins and Cooperative Calcium Alarm Signals. *Curr. Biol.* **30**, 2761-2776.e7 (2020).

20. Reátegui, E. *et al.* Microscale arrays for the profiling of start and stop signals coordinating human-neutrophil swarming. *Nature Biomedical Engineering* **1**, 0094 (2017).

21. Lämmermann, T. *et al.* Neutrophil swarms require LTB4 and integrins at sites of cell death in vivo. *Nature* **498**, 371–375 (2013).

22. Uderhardt, S., Martins, A. J., Tsang, J. S., Lämmermann, T. & Germain, R. N. Resident Macrophages Cloak Tissue Microlesions to Prevent Neutrophil-Driven Inflammatory Damage. *Cell* **177**, 541-555.e17 (2019).

23. Jiwa, K. *et al.* Immunohistochemical evidence of increased neutrophil swarms in Cystic Fibrosis lung removed at transplantation. *Eur. Respir. J.* **56**, 698 (2020).

24. Mawhin, M.-A. *et al.* Neutrophils recruited by leukotriene B4 induce features of plaque destabilization during endotoxaemia. *Cardiovasc. Res.* **114**, 1656–1666 (2018).

25. Isles, H. M. *et al.* Pioneer neutrophils release chromatin within in vivo swarms. *Elife* **10**, e68755 (2021).

26. Chtanova, T. *et al.* Dynamics of neutrophil migration in lymph nodes during infection. *Immunity* **29**, 487–496 (2008).

27. Khazen, R. *et al.* Spatiotemporal dynamics of calcium signals during neutrophil cluster formation. *Proceedings of the National Academy of Sciences* **119**, e2203855119 (2022).

28. Ng, L. G. *et al.* Visualizing the Neutrophil Response to Sterile Tissue Injury in Mouse Dermis Reveals a Three-Phase Cascade of Events. *J. Invest. Dermatol.* **131**, 2058–2068 (2011).

29. Nauseef, W. M. Human neutrophils ≠ murine neutrophils: Does it matter? *Immunol. Rev.* **314**, 442–456 (2023).

30. Siwicki, M. & Kubes, P. Neutrophils in host defense, healing, and hypersensitivity: Dynamic cells within a dynamic host. *J. Allergy Clin. Immunol.* **151**, 634–655 (2023).

31. Hopke, A. *et al.* Neutrophil swarming delays the growth of clusters of pathogenic fungi. *Nat. Commun.* **11**, 2031 (2020).

32. Molski, T. F., Naccache, P. H., Borgeat, P. & Sha'afi, R. I. Similarities in the mechanisms by which formyl-methionyl-leucyl-phenylalanine, arachidonic acid and leukotriene B4 increase calcium and sodium influxes in rabbit neutrophils. *Biochem. Biophys. Res. Commun.* **103**, 227–232 (1981).

33. Gagliardi, P. A. *et al.* Automatic detection of spatio-temporal signaling patterns in cell collectives. *J. Cell Biol.* **222**, (2023).

34. Afonso, P. V. *et al.* LTB4 Is a Signal-Relay Molecule during Neutrophil Chemotaxis. *Dev. Cell* **22**, 1079–1091 (2012).

35. McDonald, P. P., McColl, S. R., Braquet, P. & Borgeat, P. Autocrine enhancement of leukotriene synthesis by endogenous leukotriene B4 and platelet-activating factor in human neutrophils. *Br. J. Pharmacol.* **111**, 852–860 (1994).

36. Fischer, J., Gresnigt, M. S., Werz, O., Hube, B. & Garscha, U. Candida albicans-induced leukotriene biosynthesis in neutrophils is restricted to the hyphal morphology. *FASEB J.* **35**, e21820 (2021).

37. Birke, F. W., Meade, C. J., Anderskewitz, R., Speck, G. A. & Jennewein, H. M. In vitro and in vivo pharmacological characterization of BIIL 284, a novel and potent leukotriene B(4) receptor antagonist. *J. Pharmacol. Exp. Ther.* **297**, 458–466 (2001).

38. Dieterle, P. B., Min, J., Irimia, D. & Amir, A. Dynamics of diffusive cell signaling relays. *Elife* **9**, e61771 (2019).

39. McDonald, P. P., McColl, S. R., Naccache, P. H. & Borgeat, P. Activation of the human neutrophil 5-lipoxygenase by leukotriene B4. *Br. J. Pharmacol.* **107**, 226–232 (1992).

40. Wijkander, J., O'Flaherty, J. T., Nixon, A. B. & Wykle, R. L. 5-Lipoxygenase products modulate the activity of the 85-kDa phospholipase A2 in human neutrophils. *J. Biol. Chem.* **270**, 26543–26549 (1995).

41. Gilbert, N. C. *et al.* Structural and mechanistic insights into 5-lipoxygenase inhibition by natural products. *Nat. Chem. Biol.* **16**, 783–790 (2020).

42. Burke, J. R., Davern, L. B., Gregor, K. R. & Tramposch, K. M. Leukotriene B4 stimulates the release of arachidonate in human neutrophils via the action of cytosolic phospholipase A2. *Biochim. Biophys. Acta* **1359**, 80–88 (1997).

43. Surette, M. E., Krump, E., Picard, S. & Borgeat, P. Activation of leukotriene synthesis in human neutrophils by exogenous arachidonic acid: inhibition by adenosine A(2a) receptor agonists and crucial role of autocrine activation by leukotriene B(4). *Mol. Pharmacol.* **56**, 1055–1062 (1999).

44. Shaffer, B. M. Secretion of cyclic AMP induced by cyclic AMP in the cellular slime mould Dictyostelium discoideum. *Nature* **255**, 549–552 (1975).

45. van Oss, C., Panfilov, A. V., Hogeweg, P., Siegert, F. & Weijer, C. J. Spatial pattern formation during aggregation of the slime mould Dictyostelium discoideum. *J. Theor. Biol.* **181**, 203–213 (1996).

46. Gelens, L., Anderson, G. A. & Ferrell, J. E., Jr. Spatial trigger waves: positive feedback gets you a long way. *Mol. Biol. Cell* **25**, 3486–3493 (2014).

47. Krump, E., Picard, S., Mancini, J. & Borgeat, P. Suppression of leukotriene B4 biosynthesis by endogenous adenosine in ligand-activated human neutrophils. *J. Exp. Med.* **186**, 1401–1406 (1997).

48. Song, Z. *et al.* NADPH oxidase controls pulmonary neutrophil infiltration in the response to fungal cell walls by limiting LTB4. *Blood* **135**, 891–903 (2020).

49. Fiedler, J., Wheelan, P., Henson, P. M. & Murphy, R. C. Exogenous Leukotriene B4 (LTB4) Inhibits Human Neutrophil Generation of LTB4 from Endogenous Arachidonic Acid During Opsonized Zymosan Phagocytosis. **287**, 7 (1998).

50. Yang, F. *et al.* Staphylococcus aureus α-toxin impairs early neutrophil localization via electrogenic disruption of store-operated calcium entry. *Cell Rep.* **42**, 113394 (2023).

51. Serezani, C. H. C., Aronoff, D. M., Jancar, S. & Peters-Golden, M. Leukotriene B4 mediates p47phox phosphorylation and membrane translocation in polyunsaturated fatty acid-stimulated neutrophils. *J. Leukoc. Biol.* **78**, 976–984 (2005).

52. Henrickson, S. E., Jongco, A. M., Thomsen, K. F., Garabedian, E. K. & Thomsen, I. P. Noninfectious Manifestations and Complications of Chronic Granulomatous Disease. *J Pediatric Infect Dis Soc* **7**, S18–S24 (2018).

53. Roxo-Junior, P. & Simão, H. M. L. Chronic granulomatous disease: why an inflammatory disease? *Braz. J. Med. Biol. Res.* **47**, 924–928 (2014).

54. Hamasaki, T. *et al.* Leukotriene B4 metabolism in neutrophils of patients with chronic granulomatous disease: phorbol myristate acetate decreases endogenous leukotriene B4 via NADPH oxidase-dependent mechanism. *Eur. J. Clin. Invest.* **19**, 404–411 (1989).

55. Ahlin, A., Gyllenhammar, H., Ringertz, B. & Palmblad, J. Neutrophil membrane potential changes and homotypic aggregation kinetics are pH-dependent: studies of chronic granulomatous disease. *J. Lab. Clin. Med.* **125**, 392–401 (1995).

56. Tintinger, G. R., Theron, A. J., Steel, H. C. & Anderson, R. Accelerated calcium influx and hyperactivation of neutrophils in chronic granulomatous disease. *Clinical & Experimental Immunology* **123**, 254–263 (2001).

57. Henderson, L. M., Chappell, J. B. & Jones, O. T. The superoxide-generating NADPH oxidase of human neutrophils is electrogenic and associated with an H+ channel. *Biochem. J* **246**, 325–329 (1987).

58. Katikaneni, A. *et al.* Lipid peroxidation regulates long-range wound detection through 5-lipoxygenase in zebrafish. *Nat. Cell Biol.* **22**, 1049–1055 (2020).

59. Yoo, S. K., Starnes, T. W., Deng, Q. & Huttenlocher, A. Lyn is a redox sensor that mediates leukocyte wound attraction in vivo. *Nature* **480**, 109–112 (2011).

60. Ataullakhanov, F. I., Guria, G. T., Sarbash, V. I. & Volkova, R. I. Spatiotemporal dynamics of clotting and pattern formation in human blood. *Biochim. Biophys. Acta* **1425**, 453–468 (1998).

61. Lundgren, S. M. *et al.* Signaling dynamics distinguish high- and low-priority neutrophil chemoattractant receptors. *Sci. Signal.* **16**, eadd1845 (2023).

62. Perkins, R. S., Lindsay, M. A., Barnes, P. J. & Giembycz, M. A. Early signalling events implicated in leukotriene B4-induced activation of the NADPH oxidase in eosinophils: role of Ca2+, protein kinase C and phospholipases C and D. *Biochem. J* **310 ( Pt 3)**, 795–806 (1995).

63. Zinn, S. *et al.* The leukotriene B4 receptors BLT1 and BLT2 form an antagonistic sensitizing system in peripheral sensory neurons. *J. Biol. Chem.* **292**, 6123–6134 (2017).

64. Tatsumi, R. *et al.* Stepwise phosphorylation of BLT1 defines complex assemblies with β-arrestin serving distinct functions. *FASEB J.* **37**, e23213 (2023).

65. Nakanishi, Y. *et al.* Stepwise phosphorylation of leukotriene $B_4$ receptor 1 defines cellular responses to leukotriene $B_4$. *Sci. Signal.* **11**, (2018).

66. Skoge, M. *et al.* Cellular memory in eukaryotic chemotaxis. *Proc. Natl. Acad. Sci. U. S. A.* **111**, 14448–14453 (2014).

67. Geiger, J., Wessels, D. & Soll, D. R. Human polymorphonuclear leukocytes respond to waves of chemoattractant, like Dictyostelium. *Cell Motil. Cytoskeleton* **56**, 27–44 (2003).

68. Tweedy, L., Knecht, D. A., Mackay, G. M. & Insall, R. H. Self-Generated Chemoattractant Gradients: Attractant Depletion Extends the Range and Robustness of Chemotaxis. *PLoS Biol.* **14**, e1002404 (2016).

69. Aranyosi, A. J., Wong, E. A. & Irimia, D. A neutrophil treadmill to decouple spatial and temporal signals during chemotaxis. *Lab Chip* **15**, 549–556 (2015).

70. Archambault, A.-S. *et al.* 20-Hydroxy- and 20-carboxy-leukotriene (LT) B4 downregulate LTB4-mediated responses of human neutrophils and eosinophils. *J. Leukoc. Biol.* **105**, 1131–1142 (2019).

71. Pettipher, E. R., Salter, E. D., Breslow, R., Raycroft, L. & Showell, H. J. Specific inhibition of leukotriene B4 (LTB4)-induced neutrophil emigration by 20-hydroxy

LTB4: implications for the regulation of inflammatory responses. *Br. J. Pharmacol.* **110**, 423–427 (1993).

72. Noorbakhsh, J., Schwab, D. J., Sgro, A. E., Gregor, T. & Mehta, P. Modeling oscillations and spiral waves in Dictyostelium populations. *Phys. Rev. E Stat. Nonlin. Soft Matter Phys.* **91**, 062711 (2015).

73. Boldajipour, B. *et al.* Control of chemokine-guided cell migration by ligand sequestration. *Cell* **132**, 463–473 (2008).

74. Venkiteswaran, G. *et al.* Generation and dynamics of an endogenous, self-generated signaling gradient across a migrating tissue. *Cell* **155**, 674–687 (2013).

75. Tweedy, L. *et al.* Seeing around corners: Cells solve mazes and respond at a distance using attractant breakdown. *Science* **369**, (2020).

76. Insall, R. H. Receptors, enzymes and self-attraction as autocrine generators and amplifiers of chemotaxis and cell steering. *Curr. Opin. Cell Biol.* **81**, 102169 (2023).

77. Dinauer, M. C. Inflammatory consequences of inherited disorders affecting neutrophil function. *Blood* **133**, 2130–2139 (2019).

78. Song, Z., Bhattacharya, S., Clemens, R. A. & Dinauer, M. C. Molecular regulation of neutrophil swarming in health and disease: Lessons from the phagocyte oxidase. *iScience* **26**, 108034 (2023).

79. Flamand, N. *et al.* Adenosine, a potent natural suppressor of arachidonic acid release and leukotriene biosynthesis in human neutrophils. *Am. J. Respir. Crit. Care Med.* **161**, S88-94 (2000).

80. Walters, N. *et al.* Analyzing Inter-Leukocyte Communication and Migration In Vitro: Neutrophils Play an Essential Role in Monocyte Activation During Swarming. *Front. Immunol.* **12**, 1550 (2021).

81. Park, S. A., Choe, Y. H., Park, E. & Hyun, Y.-M. Real-time dynamics of neutrophil clustering in response to phototoxicity-induced cell death and tissue damage in mouse ear dermis. *Cell Adh. Migr.* **12**, 424–431 (2018).

82. Knooihuizen, S. A. I. *et al.* Loss of Coordinated Neutrophil Responses to the Human Fungal Pathogen, Candida albicans, in Patients With Cirrhosis. *Hepatol Commun* **5**, 502–515 (2021).

83. Alexander, N. J. *et al.* Neutrophil functional profiling and cytokine augmentation for patients with multiple recurrent infections: A case study. *J. Allergy Clin. Immunol. Pract.* **9**, 986–988 (2021).

84. Barros, N. *et al.* Cytokine Augmentation Reverses Transplant Recipient Neutrophil Dysfunction Against the Human Fungal Pathogen Candida albicans. *J. Infect. Dis.* **224**, 894–902 (2021).

85. Keener, J. P. Propagation of Waves in an Excitable Medium with Discrete Release Sites. *SIAM J. Appl. Math.* **61**, 317–334 (2000).

86. Kupferman, R., Mitra, P. P., Hohenberg, P. C. & Wang, S. S. Analytical calculation of intracellular calcium wave characteristics. *Biophys. J.* **72**, 2430–2444 (1997).

87. Dawson, S. P., Keizer, J. & Pearson, J. E. Fire-diffuse-fire model of dynamics of intracellular calcium waves. *Proc. Natl. Acad. Sci. U. S. A.* **96**, 6060–6063 (1999).

88. Mitkov, I., Kladko, K. & Pearson, J. E. Tunable Pinning of Burst Waves in Extended Systems with Discrete Sources. *Phys. Rev. Lett.* **81**, 5453–5456 (1998).

89. Dieterle, P. B. & Amir, A. Diffusive wave dynamics beyond the continuum limit. *Physical Review E* **104**, 014406 (2021).

90. Goroshin, S., Tang, F.-D. & Higgins, A. J. Reaction-diffusion fronts in media with spatially discrete sources. *Phys. Rev. E Stat. Nonlin. Soft Matter Phys.* **84**, 027301 (2011).

**Publishing Agreement**

It is the policy of the University to encourage open access and broad distribution of all theses, dissertations, and manuscripts. The Graduate Division will facilitate the distribution of UCSF theses, dissertations, and manuscripts to the UCSF Library for open access and distribution. UCSF will make such theses, dissertations, and manuscripts accessible to the public and will take reasonable steps to preserve these works in perpetuity.

I hereby grant the non-exclusive, perpetual right to The Regents of the University of California to reproduce, publicly display, distribute, preserve, and publish copies of my thesis, dissertation, or manuscript in any form or media, now existing or later derived, including access online for teaching, research, and public service purposes.

DocuSigned by:

*Evelyn Strickland*
—3CF63F6631BC492…          Author Signature

5/22/2024
                                             Date